FACULTY OF SCIENCE
UNIVERSITY OF COPENHAGEN

Advancing New Reconstruction Techniques For Neutrino Detectors

Master's Thesis

Author: Kasper Pedersen

Supervisors: Jason Koskinen, Tom Stuttard

Date 20/05/2021

Abstract

The IceCube neutrino observatory is sensitive to measuring neutrinos in the O(1-100) GeV regime, allowing for world-leading measurements of neutrino oscillation parameters. An essential part of maximizing the sensitivity of the oscillation analyses is being able to precisely and accurately reconstruct the parameters of the detected neutrinos. In this work, a likelihood based reconstruction method utilizing direct simulation to generate hypotheses of neutrino events has been advanced. This is done by low level testing of the generation of MC data, as well as an exploration of the quality of the likelihood space.

The current method of generating MC data is shown to build on wrong assumptions of constituents cancelling out. This issue has been resolved to create the optimal conditions for reconstruction. Even when optimizing the conditions for the likelihood space, the reconstruction method underperforms expectations when considering energy reconstruction. With a precision of 10% on average and an accuracy comparable to the seeding the energy reconstruction still remains an issue in low energy reconstruction. These issues seem to stem from the minimizer's ability to properly explore the likelihood space. The reconstruction method is shown to be a viable method of reconstructing particle parameters albeit work needs to be done before the method is competitive when compared to other current reconstruction methods. The reconstruction of the interaction vertex and azimuthal direction show very promising results, especially the reconstruction of the Z vertex is shown to perform extremely well. Here the direct simulation method reconstructs within 61 cm on average.

Future work should include further testing of the energy likelihood space and the minimization method. A lot of hidden dependencies could still be hiding just beneath the surface.

Acknowledgements

First of all a huge thank you to my supervisors Jason Koskinen and Tom Stuttard. Jason for his ability to motivate me to grind through problems like a knife through butter.
Tom for his ability to convey highly advanced scenarios in a digestible way, making it somewhat easier to jump head first into the unknown territory of particle physics and advanced programming structure.
Both of them have been a huge part in me not falling to pieces while spending 2/3 of the time locked up at home in a tiny bedroom office. Another thank you to the entire working group here at NBI, including Markus Ahlers for his curiosity at group meetings, Étienne Bourbeau for always taking the time to help with figuring out the IceCube world of programming and of course Kathrine Groth and Tania Kozynets for their office giggling, filling the hallway on the top of the M-Building with joy, as well as being there to bounce questions off of.
A huge thank you goes out to the office chums Jonathan Jegstrup and Sofus Stray for keeping the mood high and letting off steam when the programming fails to compile. A special thanks to Jonathan for all the zoom calls during lock-down discussing all our simulation and reconstruction issues.
Last but not least a thanks to the IceCube GPUs at NBI for grinding through, risking their health and well being. R.I.P node 162 (2021-05-06T18:42:23).

Author's Contribution

My contribution in this thesis has been the exploration of the photon weights and how photons are converted to hits in the simulation as well as the study on the different pulse types used in simulation in Section 5.1.4. This along with the analysis in Section 6.1 led to the removal of noise and PMT simulation from the MC simulation as well as changing the time binning method. I also did tests showing that the tolerance of the minimizer doesn't have any influence of the quality of the reconstruction. With my analysis on the zenith reconstrution in Section 6.4 it was decided to fix the zenith parameter as well as fixing time to their truth in order to create the optimal condition for the minimizer in the energy reconstruction. All analysis of the performance of the reconstruction was done by me.
Analyses on the likelihood space revealing inconsistencies that would lower the minimizers functionality was also found by yours truly.
All figures not cited are made by me.

Contents

List of Figures

List of Tables

Chapter 1

Introduction

In 1930 as an explanation for the apparent spectrum of the momentum of the electron in β decays, Wolfgang Pauli proposed a third particle, which was later named neutrino (little neutron, denoted ν) by Fermi. This explained the nonconservation of energy and angular momentum in the previous theory of two-body decay. Pauli's hypothesis wasn't confirmed until 25 years later when Reines and Cowan detected free neutrinos from β decay [1].
Today many projects around the world, are detecting this elusive fundamental particle, such as $NO\nu A$ in the USA, the $SuperKamiokande$ and $T2K$ in Japan and many more.
The most important neutrino experiment, at least for this thesis, is the IceCube Neutrino Observatory at the South Pole. So far the IceCube Collaboration has many important results to show. This includes, the measurement of ν_μ (muon neutrino) between 10-100 GeV obtaining neutrino oscillation parameters comparable to other dedicated oscillation experiments [2], improved in 2019 including the first tau neutrino appearance result in IceCube [3]. The detection of the most energetic neutrino "Big Bird" [4]. Flux limit for neutrinos from point sources [5]. In 2018, for the first time, an extremely high energy neutrino was traced back to a blazar 5.7 billion light-years away [6] and most recently in 2020 Glashow resonance predicted 60 years ago, was confirmed [7].
The ability to reconstruct properties of the particles, arriving in the IceCube detector, such as energy and incoming angle is essential for the analysis of the physics of neutrinos. The work in this thesis is dedicated to studying and advancing new reconstruction techniques for the IceCube neutrino detector. Besides the analysis of the work done, an outline of what neutrinos are and how they behave, the detector and its components along with a section on the methods used to test and advance the reconstruction of particles, including generation of Monte Carlo (MC) simulated data, is presented.

Chapter 2

Neutrinos

2.1 Properties of The Neutrino

The Standard Model of particle physics is at present the best theory that explains particle physics in terms of the interaction and properties of elementary particles (particles with no internal structure). The particles are classified by their mass, electric charge and spin etc., where particles with half-integer spin are called fermions and particles of integer spin are called bosons. The fermions are further split in two families consisting of leptons in one family and quarks in the other.
The Standard Model also describes the interactions between the particles from 3 of the 4 fundamental forces of nature: The electromagnetic interaction which binds electrons to atoms and is propagated by electric magnetic waves. The strong interaction that binds quarks inside the nucleus and the weak interaction which is the force responsible for β-decay mentioned in Chapter 1 with our beloved neutrino as a product.

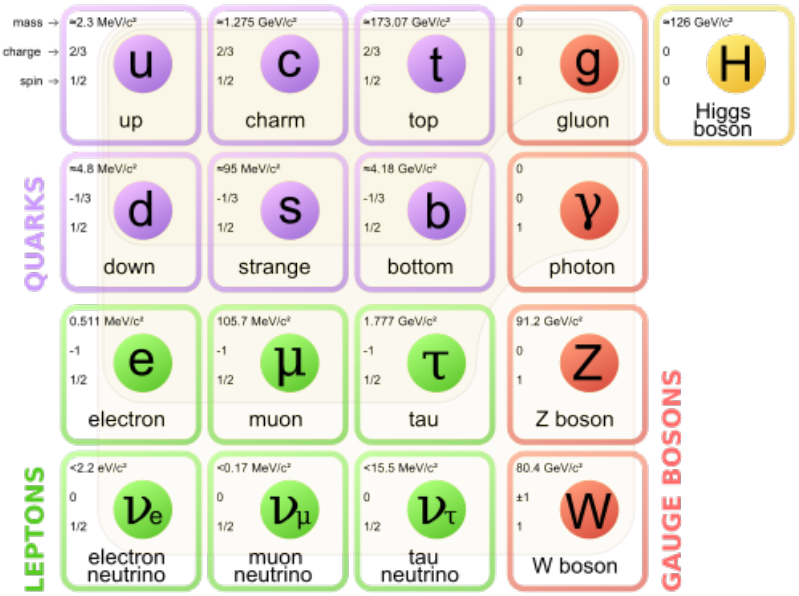

FIGURE 2.1: The Standard Model of Elementary Particles. (MissMJ, Wikipedia Commons)

As seen in Figure 2.1 the neutrino comes in three flavours. The electron neutrino ν_e, the muon neutrino ν_μ and the tau neutrino ν_τ. They come in pairs with each generation of the charged leptons, the electron, the muon and the tauon.

$$\begin{pmatrix} \nu_e \\ e^- \end{pmatrix}, \quad \begin{pmatrix} \nu_\mu \\ \mu^- \end{pmatrix}, \quad \begin{pmatrix} \nu_\tau \\ \tau^- \end{pmatrix}. \tag{2.1}$$

Contrary to the charged leptons that interact via the electromagnetic and the weak force, the neutral neutrinos have only been observed to interact via the weak force. This, and the vanishing small mass of the neutrinos, makes them very elusive and difficult to detect.

Name and symbol	Mass	Q	L_e	L_μ	L_τ	Lifetime (s)	Major decays
Electron e^-	0.511	-1	1	0	0	Stable	None
Electron neutrino ν_e	<2 eV/c^2	0	1	0	0	Stable	None
Muon μ^-	105.7	-1	0	1	0	2.197×10^{-6}	$e^-\bar{\nu}_e\nu_\mu(\sim 100\%)$ $e^-\bar{\nu}_e\nu_\mu\gamma(1.4 \pm 0.4\%)$ $e^-\bar{\nu}_e\nu_\mu e^+e^-(3.4 \pm 0.4) \times 10^{-5}$ $e^-\nu_e\bar{\nu}_\mu(< 1.2\%)$
Muon neutrino ν_μ	<0.19	0	0	1	0	Stable	None
Tau τ^-	1777.0	-1	0	0	1	2.906×10^{-13}	$\mu^-\bar{\nu}_\mu\nu_\tau(17.4\%)$ $e^-\bar{\nu}_e\nu_\tau(17.8\%)$ $\nu_\tau + hadrons(\sim 64\%)$
Tau neutrino ν_τ	<18.2	0	0	0	1	Stable	None

TABLE 2.1: Table with properties of leptons. Masses are in units of MeV/c^2. The antiparticles aren't shown and have the same mass as their counterparticles but charge (Q) and lepton number (L) have opposite sign. Neutrinos have a stable lifetime here, but neutrino oscillations are explained in Section 2.2. Table taken from [8] p.72.

In Table 2.1, properties of the leptons are shown. The neutrinos have no electric charge and are assigned a quantity called the lepton number L which equals 1 (-1 for the anti-neutrino). The lepton number is a conserved quantity and therefore needs to be conserved in interactions involving leptons. For an interaction to be allowed, the lepton number must be conserved, e.g. in nucleon-neutrino scattering

$$\nu_l + N \rightarrow l + N', \tag{2.2}$$

where ν_l is a neutrino of flavour l and N is a nucleon. The lepton number is however not universally conserved, as neutrinos have been observed to change flavour when propagating through space, known as neutrino oscillations.

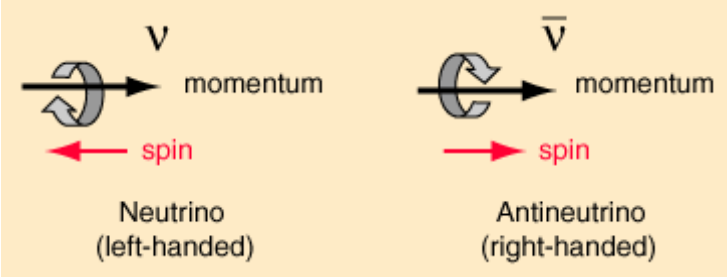

FIGURE 2.2: **Left**, a left-handed neutrino with spin pointing opposite the direction of momentum. **Right**, a right-handed antineutrino with spin pointing along the direction of momentum. Illustration from [9].

When discussing neutrinos another property of importance is the helicity-states. Here the spin of the particles is quantized along the direction of motion of the particle ie. particles with spin-$\frac{1}{2}$ has the spin component along the direction of motion of either $+\frac{\hbar}{2}$ or

$-\frac{\hbar}{2}$. The helicity states are called right- and left-handed since the direction of the spin corresponds to rotational motion in a right- or left-handed sense when viewed along the direction of momentum. This is illustrated in Figure 2.2. Only reacting through the weak force, an astonishing fact is that only left-handed neutrinos and right-handed antineutrinos are observed in nature. This fact violates C and P invariance individually but is compatible with CP invariance as the CP operator converts a left-handed neutrino into a right-handed antineutrino.

2.1.1 The Weak Force

The weak interaction, as well as the strong and electromagnetic interaction, is associated with elementary spin-1 bosons. These act as force carriers between quarks and/or leptons. The carriers of the weak force is the charged $W^{\pm}$ bosons with a charge of either plus or minus one, and the neutral Z^0 boson. Because of their charge, the $W^{\pm}$ bosons are involved in so called charged current (CC) interactions. In neutrino-nucleon scattering CC interactions is described as

$$\nu_l + N \rightarrow l + X, \tag{2.3}$$

where the neutrino ν of flavour l scattering of the nucleus, give rise to a charged lepton l and one or more hadrons X. The neutral Z^0 boson is involved in neutral current (NC) neutrino-nucleon scattering described as

$$\nu_l + N \rightarrow \nu_l + X. \tag{2.4}$$

As the name NC implies, no transfer of electric charge take part in these interactions. These carriers of the weak force is know as virtual particles as they are spontaneously created to mediate the force. With masses of $M_W = 80.4\,GeV/c^2$ and $M_Z = 91.2\,GeV/c^2$ the spontaneous appearance is violating the principle of energy conservation, and is only allowed given a very short interaction time as stated in Heisenbergs uncertainty principle $\Delta t \Delta E \geq \hbar/2$. This in turn makes the interaction length as short as $(10^{-17} - 10^{-16}\,m)$ a couple of magnitudes smaller than the charge radius of a proton.

2.2 Oscillations

In the Standard Model, the neutrinos are assumed to have zero mass albeit neutrinos have been shown to have very small mass. When having mass a weird feature of the neutrinos is neutrino oscillation where e.g. the ν_μ flavour state changes into one of the other flavour states as it transverses distances. This is under the assumption of neutrino mixing where the three neutrino flavours instead of having definite masses are linear combinations of ν_1, ν_2 and ν_3 with definitive masses meaning these states are mass eigenstates.

2.2.1 PMNS-Matrix

The Pontecorvo-Maki-Nakagawa-Sakata (PMNS) matrix [10], describes the relationship between the flavour- and mass-eigenstates as:

$$\begin{pmatrix} \nu_e \\ \nu_\mu \\ \nu_\tau \end{pmatrix} = \begin{bmatrix} U_{e1} & U_{e2} & U_{e3} \\ U_{\mu 1} & U_{\mu 2} & U_{\mu 3} \\ U_{\tau 1} & U_{\tau 2} & U_{\tau 3} \end{bmatrix} \begin{pmatrix} \nu_1 \\ \nu_2 \\ \nu_3 \end{pmatrix}. \tag{2.5}$$

Where the 3×3 matrix is the PMNS-matrix, U_{PMNS} with each term representing the mixing between the flavour ie. μ and the mass eigenstates 1,2,3. We can then write this

up as a sum for a stationary neutrino:

$$|\nu_\alpha\rangle = \sum_j U^*_{\alpha j}|\nu_j\rangle, \tag{2.6}$$

with α being one of the flavour states e, μ, τ and j the mass eigenstates $1, 2, 3$. Adding in time evolution in natural units ($c = \hbar = 1$) gives:

$$|\nu_j, t\rangle = e^{-iHt}|\nu_j, 0\rangle = e^{-iE_j t}|\nu_j, 0\rangle, \tag{2.7}$$

where H is the hamiltonian and E_j can be written as the sum of quadratures in momentum and mass. $E_j = \sqrt{p_j^2 + m_j^2}$. This can then be simplified using the binomial expansion such that terms $\left(\frac{m_j^2}{p_j^2}\right)^x$ with exponent $x > 2$ can be neglected since the mass is orders of magnitude smaller than the momentum. Furthermore the momentum doesn't need an index for the mass eigenstates anymore and since neutrinos are travelling at relativistic speed, set $t \approx L$, and the r.h.s. of Equantion 2.7 can be written as:

$$e^{-iE_j t}|\nu_j, 0\rangle \Rightarrow e^{-ipL}e^{-i\frac{m_j^2 L}{2p}}|\nu_j, 0\rangle, \tag{2.8}$$

and hence the time evolution as:

$$\sum_j U^*_{\alpha j}|\nu_j\rangle = \sum_j U^*_{\alpha j}e^{-i\frac{m_j^2 L}{2E}}|\nu_j, 0\rangle, \tag{2.9}$$

where the relativistic approximation along with $m_j \ll p$ allow us to let $p = E$. The term e^{-ipL} is a constant and is dropped since it doesn't interfere with the neutrino oscillations. Assuming the mixing matrix U is unitary and summing over all possible final flavours β the absolute square of the probability amplitude is gives the probability

$$\sum_\beta P(\nu_\alpha \to \nu_\beta) = \sum_\beta |\langle \nu_\beta, 0|\nu_\alpha, t\rangle|^2 = \sum_\beta |\sum_j U^*_{\alpha j}e^{-i\frac{m_j^2 L}{2E}}U_{\beta j}|^2, \tag{2.10}$$

$$= \sum_\beta \sum_j U^*_{\alpha j}e^{-i\frac{m_j^2 L}{2E}}U_{\beta j}\sum_i U_{\alpha i}e^{-i\frac{m_i^2 L}{2E}}U^*_{\beta i}, \tag{2.11}$$

$$= \sum_{j,i} U^*_{\alpha j}e^{-i\frac{m_j^2 L}{2E}}U_{\alpha i}e^{-i\frac{m_i^2 L}{2E}}\delta_{ji}, \tag{2.12}$$

$$= \sum_j |U_{\alpha j}|^2 = 1. \tag{2.13}$$

The probability amplitude is normalized properly and the probability for $\nu_\alpha \to \nu_\beta$ oscillation is simply its absolute square.
The trick now is to expand the sum over the mass eigenstates using $|a + b + c|^2 = |a|^2 + |b|^2 + |c|^2 + 2\Re(ab^*) + 2\Re(ac^*) + 2\Re(bc^*)$, substituting in the mass squared difference $\Delta m_{ji}^2 = m_j^2 - m_i^2$ and reducing using normalisation constraints $\sum_j U^*_{\alpha j}U_{\alpha j} = 1$ and

$\sum_{j,\alpha\neq\beta} U^*_{\alpha j} U_{\beta j} = 0$ the probability becomes:

$$P(\nu_\alpha \to \nu_\beta) = \delta_{\alpha\beta} - 4\sum_{i<j} \Re(U^*_{\alpha i} U_{\beta i} U_{\alpha j} U^*_{\beta j}) sin^2\Big(\frac{\Delta m^2_{ji} L}{4E}\Big) + 2\sum_{i<j} \Im(U^*_{\alpha i} U_{\beta i} U_{\alpha j} U^*_{\beta j}) sin\Big(\frac{\Delta m^2_{ji}}{2E}\Big). \tag{2.14}$$

Here the imaginary part doesn't contribute to neutrino oscillations but the mass squared difference in the real part is the term driving the oscillations. If $\Delta m^2_{ji} = 0$ this would make the transition probability constant for all energies and lengths. Experiments have confirmed neutrino oscillations and thereby evidence for a non-zero neutrino mass [11], [12]. The magnitude of the oscillations are described by the norm of the PMNS-matrix elements. By expanding the real part in Equation 2.14 further simplification can be made for neutrino telescopes based on measurements of values, energy resolution and sensitivity. The value of $\Delta m^2_{21} \sim 7.6 \times 10^{-5}\, eV^2$ is about 30 times smaller than $\Delta m^2_{31} \sim \Delta m^2_{32} \sim 2.4 \times 10^{-3}\, eV^2$. This combined with baselines L of atmospheric neutrinos on the order $> \mathcal{O}(1000 - 10\,000)$ km, an experimental energy sensitivity of the order $> \mathcal{O}(1)$ GeV and energy resolution of $> \mathcal{O}(0.1)$ GeV, the $sin^2\Big(\frac{\Delta m^2_{21} L}{4E}\Big)$ term becomes sub-leading and for simplicity substitute $\Delta m^2_{31} \to \Delta m^2_{32}$. When keeping the leading terms of Δm^2_{32}, the result using angles that are relevant for an atmospheric ν_μ flux is

$$P(\nu_\mu \to \nu_\mu) = 1 - 4sin^2\theta_{23}cos^2\theta_{13}(1 - sin^2\theta_{23}cos^2\theta_{13})sin^2\Big(\frac{\Delta m^2_{32} L}{4E}\Big), \tag{2.15}$$

$$P(\nu_\mu \to \nu_e) = 4sin^2\theta_{23}cos^2\theta_{13}sin^2\theta_{13}sin^2\Big(\frac{\Delta m^2_{32} L}{4E}\Big), \tag{2.16}$$

$$P(\nu_\mu \to \nu_\tau) = 4sin^2\theta_{23}cos^2\theta_{13}cos^2\theta_{23}cos^2\theta_{13}sin^2\Big(\frac{\Delta m^2_{32} L}{4E}\Big), \tag{2.17}$$

under the assumption of 3 and only 3 flavours and mass-eigenstates.
The PMNS matrix can now be expressed as

$$\begin{pmatrix} \nu_e \\ \nu_\mu \\ \nu_\tau \end{pmatrix} = \begin{bmatrix} c_{12}c_{13} & s_{12}c_{13} & s_{13}e^{-i\delta_{CP}} \\ -s_{12}c_{23} - c_{12}s_{23}s_{13}e^{i\delta_{CP}} & c_{12}c_{23} - s_{12}s_{23}s_{13}e^{i\delta_{CP}} & s_{23}c_{13} \\ s_{12}s_{23} - c_{12}c_{23}s_{13}e^{i\delta_{CP}} & c_{12}s_{23} - s_{12}s_{23}s_{13}e^{i\delta_{CP}} & c_{23}c_{13} \end{bmatrix} \begin{pmatrix} \nu_1 \\ \nu_2 \\ \nu_3 \end{pmatrix}, \tag{2.18}$$

where s_{ij} is $sin(\theta_{ij})$, c_{ij} is $cos(\theta_{ij})$ and δ_{CP} is the charge-parity violating phase factor. This matrix can then be divided into 3 sub-matrices with a long baseline as:

$$\overbrace{\begin{bmatrix} 1 & 0 & 0 \\ 0 & c_{23} & s_{23} \\ 0 & -s_{23} & c_{23} \end{bmatrix}}^{\text{Atmospheric}} \overbrace{\begin{bmatrix} c_{13} & 0 & s_{13}e^{-i\delta_{CP}} \\ 0 & 1 & 0 \\ -s_{13}e^{i\delta_{CP}} & 0 & c_{13} \end{bmatrix}}^{\text{Reactor}} \overbrace{\begin{bmatrix} c_{12} & s_{12} & 0 \\ -s_{12} & c_{12} & 0 \\ 0 & 0 & 1 \end{bmatrix}}^{\text{Solar}}, \tag{2.19}$$

giving a overview of the sources the neutrinos used to measure different parts of the mixing matrix. The atmospheric neutrinos are used in the IceCube detector to measure the $\nu_\mu \to \nu_\tau$ channel which is a direct probe of the τ-sector in the PMNS matrix and is important when testing the unitarity of the matrix as well as being the currently only feasible channel. The oscillation probability is dependent on both the energy E and the baseline L of the neutrino and the ability of precisely and accurately reconstruct these parameters

is of uttermost importance.

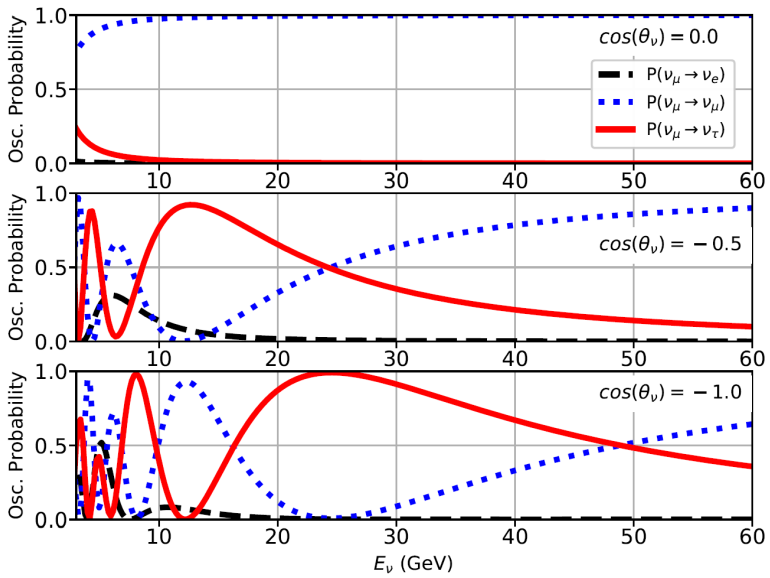

FIGURE 2.3: ν_μ oscillation probability from a 3-flavour oscillation calculation [13] and input oscillation values from [14]. The baselines are horizontal ($cos(\theta_\nu) = 0.0$),45° up-going ($cos(\theta_\nu) = -0.5$ and straight up-going ($cos(\theta_\nu) = -1.0$)). Figure courtesy of D. Jason Koskinen.

In IceCube the baseline L directly translates into the zenith angle θ_ν of the incoming atmospheric neutrino and Figure 2.3 shows the the ν_μ oscillation probability for three baselines of horizontal, 45° up-going and straight up-going neutrinos. This again underlines the importance of the ability of determining the energy and baseline to measure the oscillations that is measurable with low energy neutrinos.

2.3 Detection

The neutrinos detected in IceCube are mainly atmospheric neutrinos. These come from showers of particles produced when cosmic rays interact with atomic nuclei in Earth's atmosphere. Cosmic rays are high energetic particle, typically protons, coming from sources such as supernovae and active galactic nuclei (AGN). Cosmic rays interacting with the nuclei in Earth's upper atmosphere, produces a lot of short-lived mesons such as the Kaon and Pion, most of which are Pions. The mesons then rapidly decay into μ and $\bar{\nu}_\mu$ or their equivalent anti particles. For the Pion this happens in $\sim$ 99.9% of all decays. The μ then decays into $e^- \bar{\nu}_e \nu_\mu$ meaning that about 2/3 of atmospheric neutrinos are ν_μ and $\bar{\nu}_\mu$ and 1/3 is ν_e and $\bar{\nu}_e$. Deviation from this ratio has provided evidence for neutrino oscillations.
By measuring atmospheric neutrinos coming from all directions, the position of IceCube at the South Pole makes it possible to detect neutrinos at a wide range of baselines. The incoming angle θ_ν directly translates into a baseline L to the point on the atmosphere where the neutrino has intersected the Earth.
The illusive nature of neutrinos makes them impossible to detect directly and they don't give away any sign of presence unless they interact with something. They way to detect neutrinos i.e. in IceCube is by recording the light from charged particles created

by neutrinos interacting in ice, producing Čerenkov radiation. The IceCube detector is immersed in glacial ice which is extremely clear at depths below 2100 m. The ice isn't complete homogeneous as ice properties has been found to vary with depth with high concentrations of mineral dust, correlated with climatological history. The majority of dust is found between depths of 2000-2100 m and is called the dust layer. The bottom region of the detector has specifically been designed to avoid the highly scattering and absorbing ice in the dust layer. The ice below 2100 m has been found to be $40\% - 50\%$ more clear on average with an average effective scattering of 50 m and an average absorption length of 190 m. The values cited are measured using 400 nm light which is the wavelength where absorption due to dust is weakest and the ice shows most transparency. This is also the wavelength near the peak sensitivity of the detector [15].

2.3.1 Čerenkov Radiation

When a charged particle travels in a medium of refractive index n, it will polarize atoms in the medium which will radiate coherent light. If the particle travels with a velocity v greater than that of the speed of light in the medium the light is emitted at a characteristic angle θ to the direction of motion of the particle and thus creates a characteristic wavefront. This condition $v > c/n$ and using Huygen's principle can be shown that $cos(\theta) = 1/\beta n$, where $\beta = v/n$. The number of photons radiated per unit path length in wavelength interval $d\lambda$ is given by:

$$N(\lambda)d\lambda = 2\pi\alpha\big(1 - \frac{1}{\beta^2 n^2}\big)\frac{d\lambda}{\lambda^2} < 2\pi\alpha\big(1 - \frac{1}{n^2}\big)\frac{d\lambda}{\lambda^2}. \tag{2.20}$$

The number of photons emitted decreases rapidly with refraction index approaching 1 so a great number of events are needed in order to collect enough data.

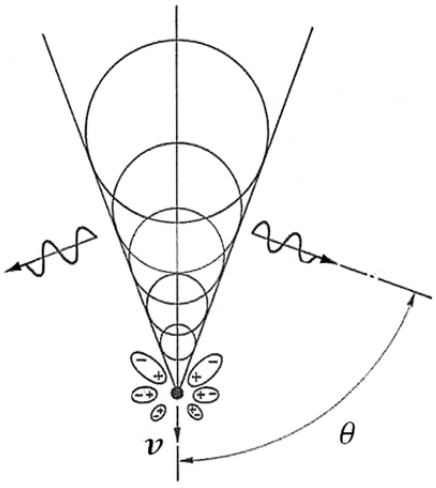

FIGURE 2.4: Schematic of Čerenkov Radiation for a charged particle travelling at $v > c/n$. Figure from [16].

2.3.2 Showertypes

When neutrinos interact with nuclei in the ice within the IceCube detector, the interaction produces charged particles that produce the Čerenkov radiation that is detected. The radiated light has wavelengths in the low energy spectrum of ultra-violet (UV) light into visible blue light. The energy and momentum of these charged particles reflect the energy

and momentum of the original neutrino i.e. the light produced by these showers are maximal and has low variance and forms a natural unit of the energy of a reconstructed shower. The neutrino energy resolution is then only limited by the detector resolution for identified CC interactions. The events in IceCube have two distinct topologies. Tracks that are formed mostly by muons from either cosmic ray showers or ν_μ CC interactions and cascades which are events with no visible muon tracks. The latter is produced in ν_e CC and in all flavour NC events.

Interaction	Topology
$\nu_e + N \rightarrow e + had.$	Cascade
$\nu_\mu + N \rightarrow \mu + had.$	Track(+ Cascade)
$\nu_\tau + N \rightarrow \tau + had. \rightarrow had.$	Cascade/Double Bang
$\nu_\tau + N \rightarrow \tau + had. \rightarrow \mu + had.$	Cascade + Track
$\nu_l + N \rightarrow \nu_l + had.$	Cascade

TABLE 2.2: Different interactions and signature of events in IceCube. Top section shows CC interactions while NC are shown in the bottom line. Table taken from [17] p.3.

In Table 2.2 the 4 top rows show the CC interactions and the bottom row shows the NC interaction in IceCube. In CC interactions almost all of the primary neutrino energy is deposited into the lepton and in the hadronic shower while in the NC interaction a lot of the deposited energy is transferred to the outgoing neutrino.

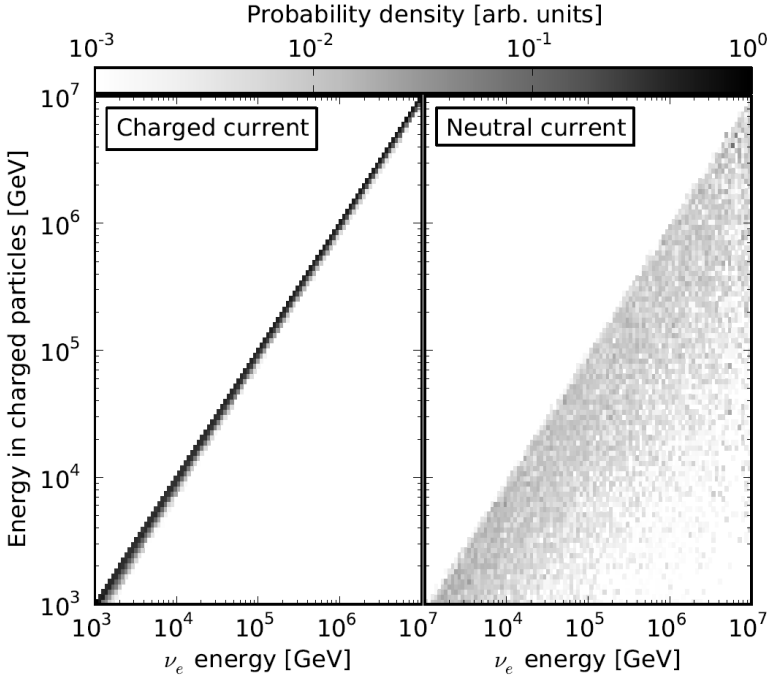

FIGURE 2.5: Energy deposited in charged particles by ν_e scattering in ice. Left plot shows the linear relationship in CC interactions with very little variance. Right plot is for NC interactions that show a huge variance from energy losses. Figure from [17].

Fig 2.5 shows the relation between the neutrino energy and the deposited energy in charged particles in ice [17].

Chapter 3

IceCube Neutrino Observatory

In December 2010, the largest particle detector the world has seen, was finished after many years of preparation by the IceCube Collaboration, which consists of more than 300 scientists from 49 institutions and 12 countries. The detector is embedded in one cubic kilometre of ice at the geographical South Pole and thousands of digital optical modules (DOMs) are located between 1450-2450 meters beneath the surface. The detector consists of 86 strings each with 60 DOMs attached 17 meters apart [18]. The center of the bottom part (2100-2450 meters) of the detector, called DeepCore consists of DOMs attached only 7 meters apart [15].

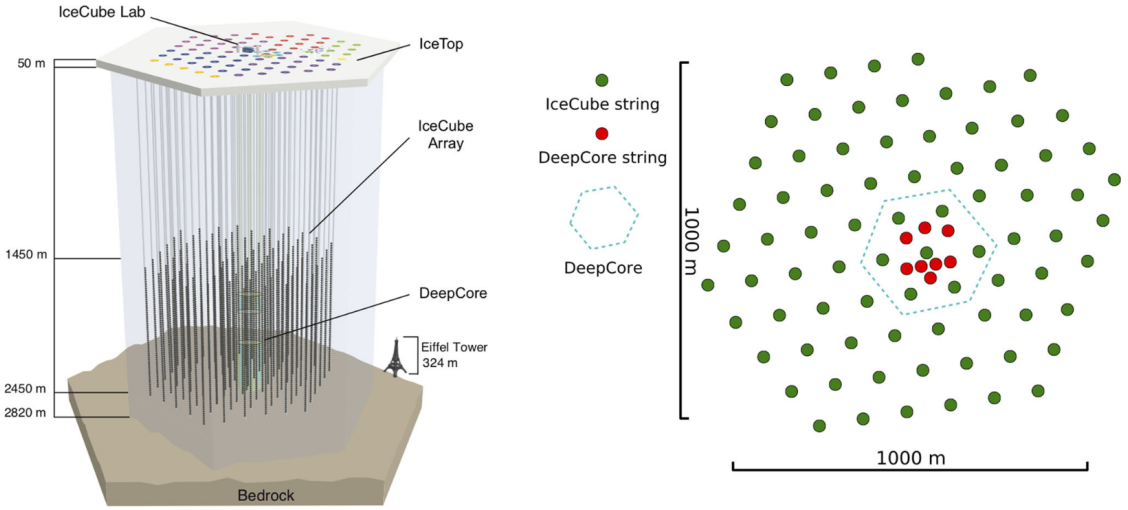

FIGURE 3.1: **Left** Layout of the IceCube Neutrino Observatory. **Right** The detector seen from the top. Figure from [19].

An illustration of the observaroty is seen in Figure 3.1. The majority of the DOMs in DeepCore are high quantum efficiency (HQE) DOMs, all other DOMs are referred to as normal quantum efficiency (NQE) DOMs. This more dense region of the detector is sensitive to neutrinos with energies lower than 100 GeV. In the near future, work will begin to deploy more strings with new types of DOMs at lesser spacing to improve the sensitivity even further. The events IceCube detects come from air showers of particles in IceTop and penetrating μ detection in DeepCore where the events are dominated by cosmic ray μ by a factor of $\approx 10^6$ for every neutrino. An event in IceCube lingo is a particle interacting with the ice and leaving a detectable trace in the detector.

3.1 The DOM

The DOMs used by IceCube each contain a photo-multiplier tube (PMT) for detecting Čerenkov radiation, a mu metal grid to shield the PMT from the magnetic field of the earth, a gel layer that optically couples the glass of the PMT to the glass pressure housing, a mainboard containing all the onboard processor and electronics, a light emitting diode (LED) flasher board used for calibration and a high voltage (HV) divider that supplies the PMT with the correct voltages.

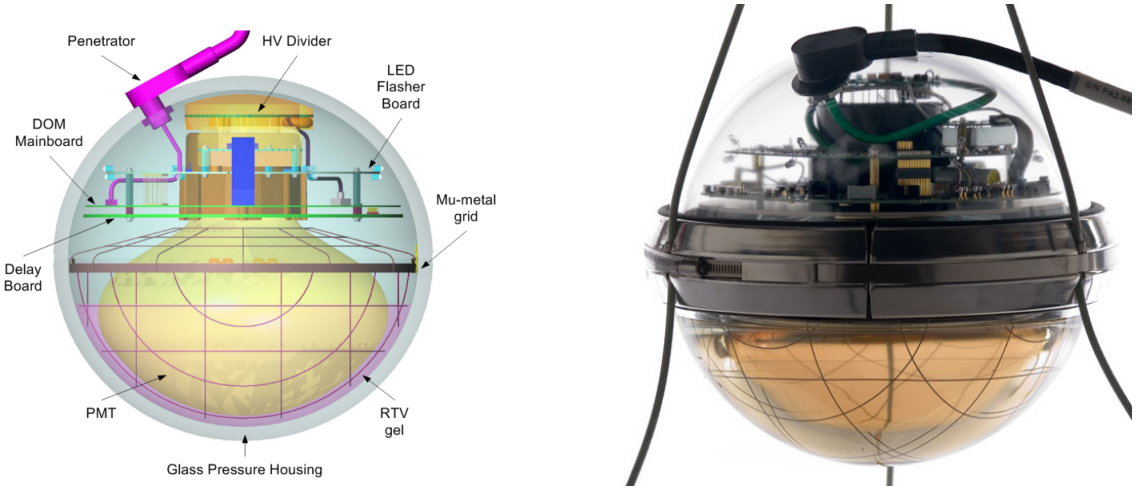

(A) Components of a DOM

(B) Picture of a DOM

FIGURE 3.2: (A) Shows the schematic of a DOM [20]. (B) Shows an actual image of a DOM [21].

These components can be seen in Figure 3.2a. The spherical pressure housing is well known in other lines of research where reliability against implosion must be ensured. The DOMs are 13" in diameter and the borosilicate glass used in the DOMs has a transmission limit $\sim$ 350 nm low enough to let the Čerenkov radiation through. Each DOM is connected to the IceCube Laboratory at the surface through a single cable and also has two wire pairs connecting each DOM to it's two neighboring DOMs. This is done to observe local coincidence described in Section 3.1.3.

3.1.1 PMT

To convert the received light into an electric signal, DOMs are equipped with a halfspherical 10" PMT. HQE DOMs are equipped with high quantum efficiency (HQE) PMTs. Measurements done in laboratory show a 39% higher optical sensitivity compared to NQE DOMs at a wavelength of 405 nm. *In situ* measurements show an improvement of 35% smaller than what was measured in the laboratory possibly due to the Čerenkov spectrum not being monochromatic and optical properties of the ice surrounding the DOMs. HQE DOMs has an average noise rate higher by a factor of 1.33, at $-45°C$, compared to NQE DOMs. Simulations demonstrate the added efficiency to increase the effective area of DeepCore triggering on low energy neutrino events by 30% [15]. A schematic of a general PMT is shown in Figure 3.3. When light hits the photocathode, an exited eletron called photoelectron (PE), is emitted by the photoelectric effect. Focusing electrodes will guide the accelerated electron into the electron multiplier. This is made of a series of dynodes where the electron generates multiple secondary electrons which in

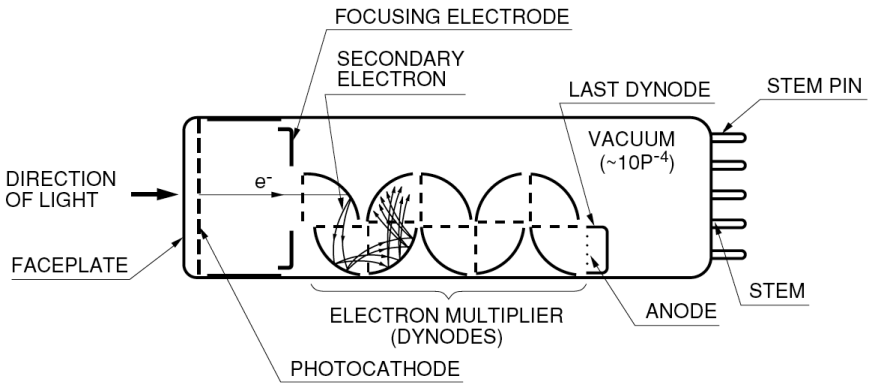

FIGURE 3.3: General Schematic of a PMT. IceCube PMTs consists of 10 dynodes, has a wavelength range of $300 - 550$ nm, a transit time of 60 ± 3 ns and a cathode area of $470 - 530$ cm^2[22].

turn are accelerated onto the next dynode. Finally an anode will collect the amplified signal from the electron cascade yielding a gain of $\sim 10^7$.
Beside photoelectrons the PMT is subject to prepulsing, afterpulsing and latepulsing. Prepulses are small amplitude pulses from photons entering the PMT producing PEs from the first dynode. Prepulses appear before the main body of PE pulses. Afterpulses occur when PEs ionize residual gas atoms, in the PMT, which due to their positive charge drift back to the photocathode and dislodge several electrons. Latepulses happen when an electron scatters back from the first dynode. It takes some time for it to reach the dynode again and produce what is called a latepulse.

3.1.2 Data Aquisition

The DOM mainboard contains the electronics to amplify and digitize the signal gained from the PMT. The waveform digitization starts when the signal of the PMT exceeds a discriminator threshold of 0.25 PE using an analog transient waveform digitizer (ATWD). The readout window for the ATWD is $427\,ns$. The digitization process takes $\sim 29\,\mu sec$ during which another waveform can't be digitized. To overcome this issue 2 ATWD chips (A and B) are used sequentially i.e. after a waveform has been captured on chip A, chip B will capture the next waveform and so forth. By applying this method there is virtually no deadtime in the data aquisition. The ATWD chips have 4 10-bit resolution read-out channels where the 3 first are used for different gain and the fourth is used internally for calibration. Each channel captures 128 samples before trigger conditions determine to digitize the signal or not. A typical PE has a charge of $5 - 8$ mV. In addition to the ATWDs, the mainboard also contains a fast analog to digital converter FADC. This pipelined output is capable of capturing signals that outlast the timespan of the ATWDs. The FADC continuously samples an PMT output signal and has $6\,\mu s$ readout window. [23].

3.1.3 Local Coincidence

When the PMT signal exceeds the discriminator threshold the waveform captured by the ATWD will only be digitized if a neighboring og next to nearest neighbor DOM registers a signal which also exceeds the 0.25 PE threshold within $\pm 1\,\mu sec$. This is called "local

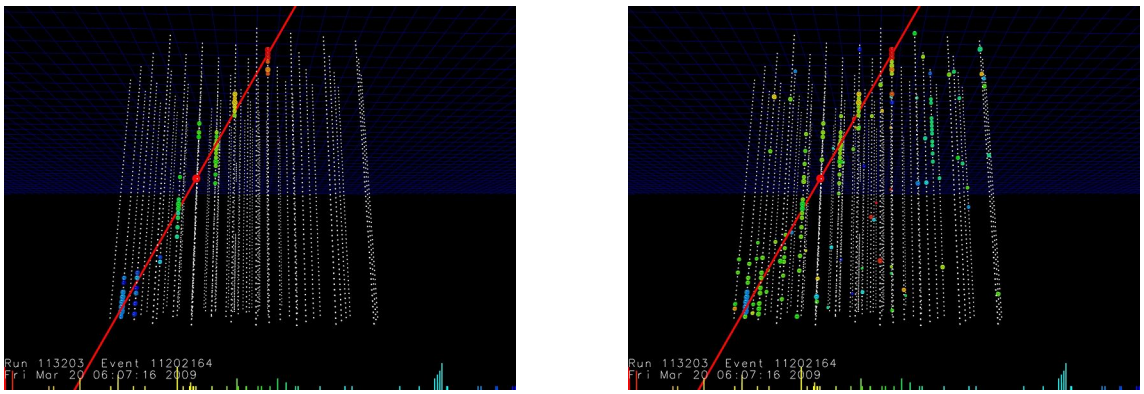

(A) HLC (B) SLC and HLC

FIGURE 3.4: (A) Example of an event with HLC only . (B) Example of an event with both SLC and HLC [24].

coincidence" (LC). Furthermore there a two types of readouts illustrated in Figure 3.4. Hard local coincidence (HLC) requires every signal to have a LC tag thereby discarding all PMT triggers without a tag and heavily reducing the data input. HLC signals are collected using both the ATWD and the FADC chip, and contains a lot of information making up for the worse time resolution of the FADC. Soft local coincidence (SLC) is signals that aren't HLC. SLC only uses the FADC as readout, which is possible from the near zero deadtime, from the fast digitization of FADC. SLC signals will then contain less information of the features of the pulse received, however still useful. [23].

3.2 Neutrino Oscillations in IceCube

Neutrino oscillations are measured in IceCube by probing the $|U_{\tau 3}|^2$ matrix element of the PMNS-matrix described in section 2.2.1. In principle one can use the $\nu_e \rightarrow \nu_\tau$,$\nu_\tau \rightarrow \nu_\tau$ and the $\nu_\mu \rightarrow \nu_\tau$ channels. The two first are undesirable. The first because of the low magnitude of oscillation and ν_e and ν_τ produce a similar signature experimentally. The second is challenging as it requires an unrealized high-stats focused ν_τ beam. The most feasible channel in practice is the $\nu_\mu \rightarrow \nu_\tau$ channel which probes both $|U_{\mu 3}|^2$ and $|U_{\tau 3}|^2$.

A benefit of the location of the IceCube detector is the ability to measure atmospheric neutrinos generated at all zenith angles, θ_ν at a range of baselines L, ranging from $\sim$ 10 km to the diameter of the earth. From directly down going from above the detector ($cos(\theta_\nu) = 1$) to directly up going from the opposite side of the earth ($cos(\theta_\nu) = -1$). This gives a wide range a combinations of base length and energy (L/E) to study neutrino oscillations. As seen in fig 3.5, the first peak of maximal $P(\nu_\mu \rightarrow \nu_\tau)$ is around 25 GeV for directly up going neutrinos [3]. Neutrinos at these energies do not disperse much energy in the detector and makes it even harder to reconstruct the parameters of the incoming neutrinos in the detector.

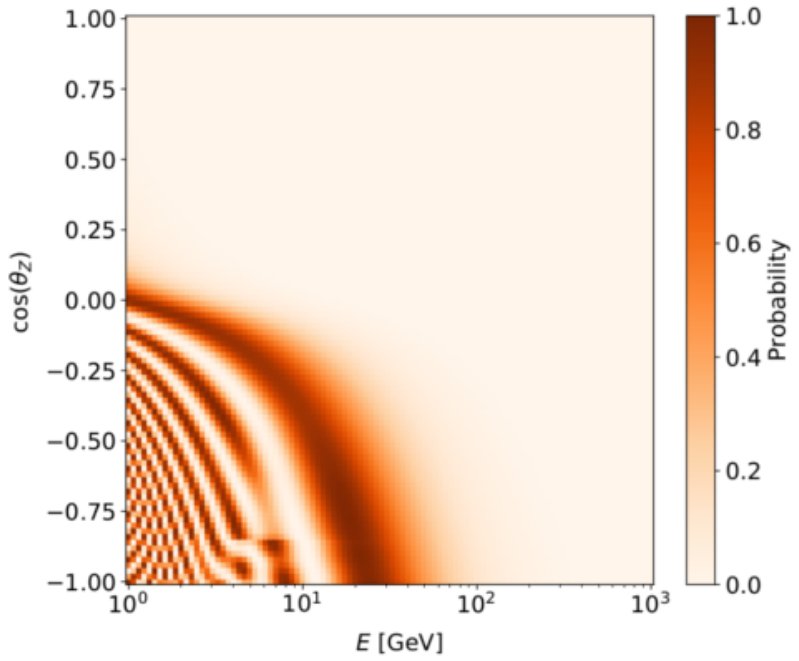

FIGURE 3.5: Plot showing the oscillation probability of a ν_μ reaching IceCube. A neutrino produced in particle shower will travel along different baselines of the earth depending on it's zenith angle. The oscillation probability therefore depends on it's energy and effective travel length. Figure from [25].

Chapter 4

Direct Reconstruction

Finding the energy, position, direction and type of neutrino, is hard for low energy events. They don't leave much information in the detector as less DOMs see photons from low energy interactions in the ice.

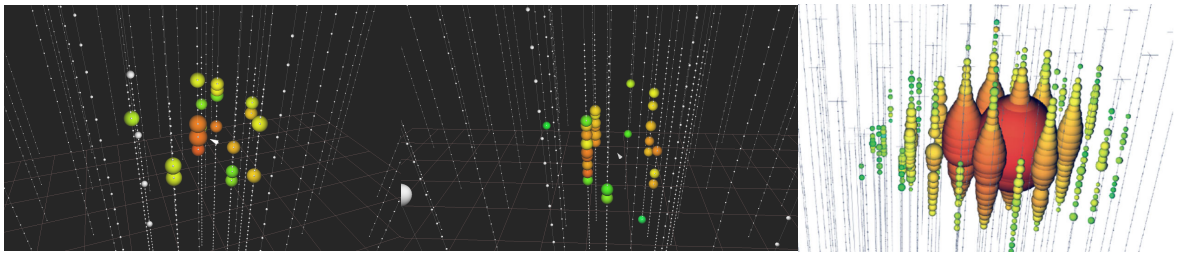

(A) (B) (C)

FIGURE 4.1: The figures shown examples of cascade events in DeepCore. Each grey dot is a DOM and the size is proportional to the amount of charge received. The color indicate the time of triggering range from early time in red to late time in blue. The grey arrow is the interaction vertex and direction. **(A)** Is a 14 GeV e^- simulated in the center of DeepCore. **(B)** Is a 26 GeV e^- simulated in the ceneter of DeepCore. **(C)** Is a high energy cascade taken from [19].

Figure 4.1 shows three examples of the amount of information in the detector. **(A)** and **(B)** is a simulated e^- in the center of DeepCore with energies 14 and 26 GeV respectively while **(C)** shows a high energy ν_e or ν_τ CC event. These examples points out the difference in information in the detector when working with low energy events. The goal of DirectReco (Direct Reconstruction) is to replace the current method of table lookup which is pre-generated tables that describe the probability of detecting photons for cascades or muons and characterizing the propagation of photons through the ice. The tables are created using a 1 GeV hypothesis and then scaled accordingly when reconstructing. The downsides of table lookup include the computational time producing and verifying them. Currently when using some of the best methods for low energy reconstruction, the table lookup is a dominant factor in memory usage and reconstruction time. Another issue is that the tables are specific to individual icemodels. IceCube always wants to use the most recent icemodel and generating and verifying new tables is a multi-year process, making publishing impossible in that time window. DirectReco sees to this issue by performing realtime photon propagation and directly simulates the hypothesis events (Schematic in Figure 4.2a) and then utilize the millipede reconstruction framework. This makes DirectReco very flexible and it is easy to implement different ice-models, vary the minimizer used and its settings, determine which oversampling is used and to use different likelihood calculations etc. The time of reconstruction in DirectReco is hence limited by photon propagation time.

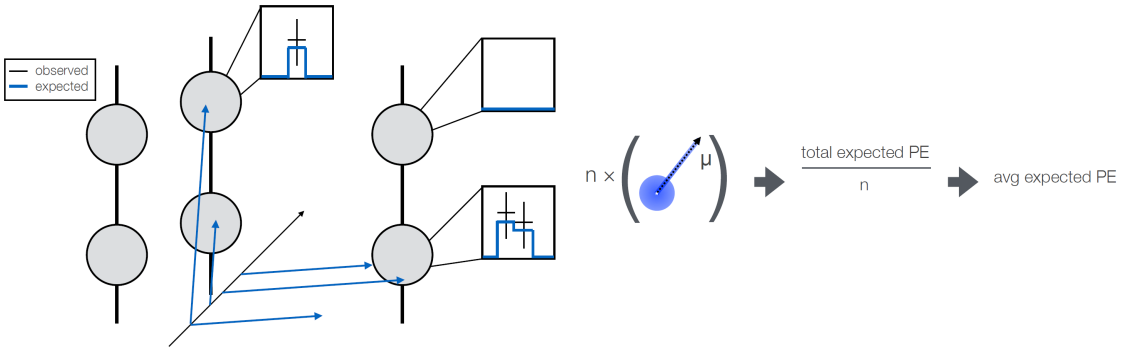

(A) DirectReco Schematic (B) DirectReco Oversampling

FIGURE 4.2: (A) Schematic of event hypotheses in DirectReco. A particle is simulated and an expected charge is calculated. The grey circles represents DOMs. The black line is a charged particle transversing the ice producing Čerenkov photons represented by the blue lines. The squares show the waveform of the pulses received by the DOMs with the black points being the observed charge and the blue histograms the expected charge from the hypothesis. (B) Schematic of oversampling. The particle is simulated n times and normalized to get an expected average charge and minimize statistical fluctuations. Source: Sarah Nowicki, IceCube Internal Talk.

Specifically the oversampling is important in DirectReco. Here each particle is propagated n times and the expected charge is the normalized to minimize the statistical fluctuations as described in 4.2b. This is all handled in the framework *Millipede* where the best values of the reconstructed parameters are found by estimating the negative log likelihood space. The returned values are the parameters giving the minimum of the negative 7-D log likelihood landscape. The parameters being reconstructed are energy, zenith angle, azimuthal angle, position of the interaction vertex (x,y,z) and time of interaction.

4.1 Millipede

Millipede is a toolkit for reconstruction developed by IceCube. Usually Millipede is reconstructing μ tracks in the detector by dividing the track into segments hence the name Millipede. In this work a segment of Millipede called Monopod is used. Monopod is useful when reconstructing cascades and is basically a single tracksegment of Millipede but still uses the Millipede framework. Millipede includes a wide range of different minimizers to be used in reconstruction as well as handling the time binning of the input from the event that is to be reconstructed.

4.1.1 Likelihood Model

The energy reconstruction in IceCube is based on the linearity of the light yielded in CC and NC events along with the calculation of expected energy losses. This scaling makes it possible to use EM and hadronic showers as fundamental units of energy reconstruction. This is done by scaling the expected light yield of a template (simulated event) to match the observed data. The deposited energy is then estimated by comparing the number of photons in a photon multiplier tube (PMT), which is described in Section 3.1.1, k to the expected light yield Λ for a template event that is either tabulated or directly simulated (templates such as the SPE template are described in chapter 4). The number of photons observed follows a Poisson distribution with a mean of $\lambda = \Lambda E$ and the likelihood $\mathcal{L}$ for

a given energy E to result in k detected photons from an event that produces Λ photons per unit energy is:

$$\mathcal{L} = \frac{\lambda^k}{k!} \cdot e^{-\lambda}, \tag{4.1}$$

$$\lambda \to E\Lambda, \tag{4.2}$$

$$= \frac{(E\Lambda)^k}{k!} \cdot e^{-E\Lambda}, \tag{4.3}$$

$$\ln \mathcal{L} = k \ln(E\Lambda) - E\Lambda - \ln . \tag{4.4}$$

Then by adding contributions from all digital optical modules (DOMs) j, and maximizing the expression wrt. E gives:

$$0 = \frac{\partial \sum \ln \mathcal{L}}{\partial E} = \sum_j (k_j \Lambda_j / E\Lambda_j - \Lambda_j), \tag{4.5}$$

$$= \sum k_j / E - \sum \Lambda_j, \tag{4.6}$$

$$\to E = \sum k_j / \sum \Lambda_j. \tag{4.7}$$

In reality there will also be noise photons such as PMT noise. Noise is the added in by letting $\lambda = E\Lambda \to \lambda = E\Lambda + \rho$ where ρ is the expected noise photons. Substituting in noise gives the log likelihood:

$$\ln \mathcal{L} = k \ln(E\Lambda + \rho) - (E\Lambda + \rho) - \ln(k!), \tag{4.8}$$

and again maximizing wrt. E gives:

$$\sum \Lambda_j = \sum k_j \Lambda_j / (E\Lambda_j + \rho_j). \tag{4.9}$$

When adding noise the expected light yield doesn't cancel out and it is not possible to get a solution for E. This can be obtained by using numerical minimization algoritms [17]. Millipede is able to use two different likelihood models. The default is a Poisson Likelihood:

$$\ln \mathcal{L} = \sum_{N_{bins}} d_i \ln(s_i) - s_i - \ln \Gamma(d_i + 1), \tag{4.10}$$

where d_i is the charge in the i'th bin and s_i is the expected charge from the hypothesis and $\ln \Gamma$ is the natural log of the gamma function. The default Poisson likelihood is used by table reconstruction whereas DirectReco uses the Dima likelihood that accounts for model errors and weighted simulation [†] and is named after its creator [26]. For large oversampling the Dima likelihood is expected to converge towards the Poisson likelihood. The only weighting available in DirectReco is the oversampling factor which is the same for each bin and not a distribution. The Dima likelihood for DirectReco is defined as:

$$\begin{aligned} \ln \mathcal{L}_{Dima} &= n_s s_i \ln(\mu_i / s_i) + n_d d_i \ln(\mu_i / d_i), \\ \mu_i &= \frac{n_s s_i + n_d d_i}{n_s + n_d}, \end{aligned} \tag{4.11}$$

[†]Model errors relates to simplifications when performing finite element model analysis e.g. geometry approximations, boundary conditions etc. and is a measure of the amount of disagreement between data ans simulation.
Weighted simulation refers to multiple simulation points within the same bin being weighted.

where d_i and s_i are respectively the observed and the expected charge in the i'th bin, n_d is the number of "data trials" which is 1 for DirectReco and n_s is the number of "simulation trials" i.e. the oversampling factor. As mentioned above the computational time of a reconstruction depends on the oversampling and it is therefore necessary to find a compromise between computational time and accuracy and precision of the reconstructed parameters.

4.1.2 Millipede Binning

The input data from the event given to Millipede, consists of a set of pulses, each with a varying width and charge (amplitude) for each DOM. Millipede then bins the data based on several user inputs. Options are available to put all pulses in a single time bin, dynamic binning, choosing a maximum number of pulses in each time bin and uniform time binning where the width of the bins is the same for all bins and set by the user.

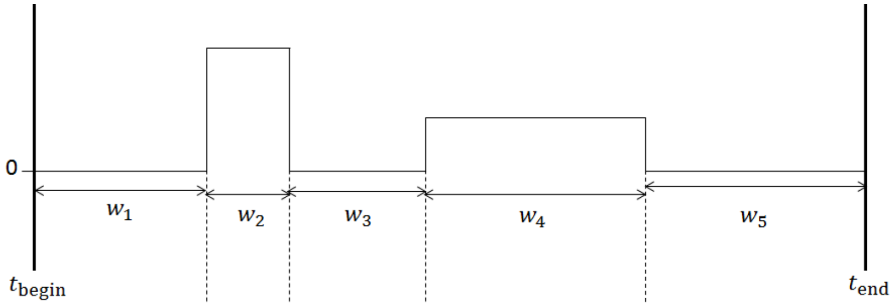

FIGURE 4.3: Simple Millipede binning example where two pulses of widths w_2 and w_4 is binned. Figure from [27].

Figure 4.3 shows an example of dynamic binning. It shows two pulses of widths w_2 and w_4 being binned into 5 bins. The empty bins of width w_1 and w_5 will typically be much larger because the readout window is much larger than the pulse series.

4.1.3 Simplex algorithm

The minimum of the negative loglikelihood landscape for a given event will give the most likely parameters for that event. The default minimization algorithm in Millipede is the simplex algorithm [28]. This algorithm is a part of the *Minuit* package developed by people at CERN. It performs minimization using the simplex method developed by Nelder and Mead. This direct search method is designed to minimize a given nonlinear function $f : \mathbb{R}^n \rightarrow \mathbb{R}$. It only uses function values at some points in the n-dimensional likelihoodspace $\mathbb{R}^n$ and does not approximate any gradient at any of said points. A simplex is defined as the convex hull of $n+1$ vertices, ie. in 2D the simplex is a triangle, in 3D a tetrahedron and so forth. The simplex performs a sequence of transformations trying to minimize the function values at the vertices determining the transformation at each step of the sequence by comparing the current function values with values at a sample of one or more test points. The algorithm terminates after it has reached approximately a number of maximum function calls, given by user or when the simplex gets small in some sense or the computed function values are close enough using a tolerance input. One of the advantages of the simplex method is its ability to converge fast, typically only requiring a few function evaluations at each iteration. A caveat is that it also can take a huge number of iterations with no, to little improvement, in the function value despite being no way near the true minimum [29].

Chapter 5

Generating MC Data

5.1 MC Simulation

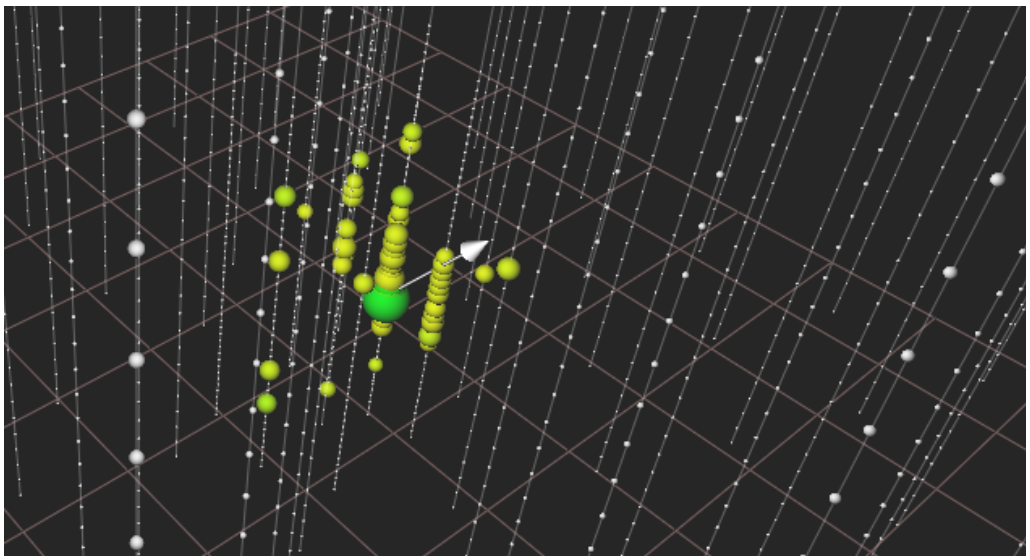

FIGURE 5.1: Visual from the event viewer of one of the events of the simulated 50 GeV e^-. The grey arrow shows the direction of the event. The coloured balls are hit DOMs with size corresponding to the number of pulses received. The colouring shows the time of the hits ranging from green to red.

The MC data used in this work to be able to perform low-level testing of the hypothesis generation in *Millipede* is made by simulating an ideal event of a 50 GeV electron cascade in the middle of DeepCore, approximately 10 000 times. Figure 5.1 shows a example of one of the simulated events. Simulating the same electron for each event (same vertex, angle and energy) will cancel out any randomness from the individual events when analysing the average behavior. The truth seed is then used to generate a hypothesis in millipede which is compared to the averaged event.

5.1.1 Simulation Chain

The simulation chain used to generate the MC data is divided into 5 parts.

Step 1

- An 50 GeV e^- is created at vertex = (37 m,-73 m,-380 m), θ_{zenith} = 143.13 deg, $\phi_{azimuth}$ = 0 deg, 10 000 times.

Step 2

to the detector and the photons from the resulting Čerenkov radiation are propagated in the ice until either absorbed or at a DOM.

Step 3

- The photon hits on a DOM are converted into MCPE (Monte Carlo Photo Electrons).
- Noise is added using the *Vuvuzuela* module.
- The photo electrons are given a charge using Rosencrantz (PMTSimulator) and Guildenstern (DOMLauncher).

Level 1

- Triggering.

Level 2

- Filtering.

5.1.2 Step 1

In general, when creating particles in step 1, one uses a dedicated generator like *GENIE* [30]. In this work, a toy MC has been used to perform testing at lower levels of DirectReco. Here the 50 GeV e^-, is added as a primary particle for each event.

5.1.3 Step 2

The photon propagation in step 2 is done using *CLSim* that utilizes *GEANT4* which is a toolkit for simulating particles transversing matter. Here *GEANT4* handles the transport of the non-photon particles while *CLSim* propagates the Čerenkov photons from the charged e^-. No light propagation is started if it is more than 300 meters way from a DOM. The Čerenkov photons are created with a bias in photon wavelength, added to reflect the wavelength spectrum of the Čerenkov radiation. If a photon hits a DOM it is saved with attributes *Time*,*Weight*,*Wavelength*,*Direction*,*Position*,*Group Velocity* and *Particle ID*.
Figure 5.2 shows the distribution of weights given to photons compared to the DOM wavelength acceptance curve. In order to match the acceptance curve to the photon weights, it is calculated using an efficiency of the product between the unshadowed fraction = 1, the maximum angular acceptance of the *angsens/as.h2-50cm* hole ice parameterization, the relative DOM efficiency (RDE) and a compensation factor from the SPE template (SPE templates are described below in section on PMT simulation). When DOMs are embedded in the ice by drilling holes with hot water, the column of refrozen ice is referred to as the hole ice. It is believed that the hole ice contains air bubbles from the refreezing that makes this ice more scattering. This modifies the angular sensitivity of the DOM by increasing the probability for downgoing photons which would otherwise pass the DOM to scatter into the PMT.
The RDE stems from the HQE DOMs effectively seeing more charge than the NQE DOMs. SPE templates effectively change the amount of charge per photo electron and hence shifts the DOM efficiency, and the compensation factor is brought in to compensate for this shift. The hole ice, RDE, compensation factor and the unshadowed fraction, don't change the shape of the distribution, but merely work as a scaling factor, combined. It is worth noticing the extreme fluctuation around 300 nm on the left plot of Figure 5.2. The

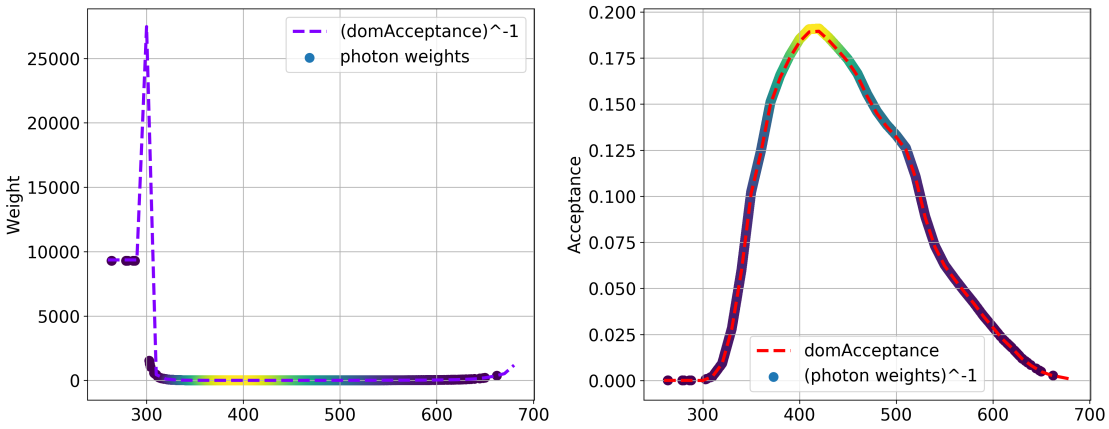

FIGURE 5.2: Figure showing the relationship between the DOM wavelength acceptance curve and the distribution of weights given to photons in simulation. Left shows the distribution of the photon weights coloured by density (yellow high density, blue low density) overlaid by the inverse the DOM acceptance curve (purple dashed line). Right shows the DOM acceptance curve (red dashed line) with the inverse photon weights.

weights are expected to get higher below 300 nm but in a smooth transition to approximately 10 000. This is a consequence of the extrapolation made to smooth out the low wavelength end of the DOM acceptance curve. This looks fine until using the inverse as is the case here.

5.1.4 Step 3

Photon Conversion

The photons saved in step 2 are given to the *CLSim* module *I3CLSimMakeHitsFromPhotons*. This module calculates the wavelength acceptance (*domAcceptance*) with efficiency of $icemodel\_efficiency\_factor \times UnshadowedFraction$ using the *spice-3.2.1* ice model and an unshadowed fraction of 1. The angular acceptance (*domAngularSensitivity*) is calculated using the Hole Ice Parameterization from *angsens/as.flasher_p1_0.30_p2_-1* hole ice. These are then used in the module *I3PhotonToMCPEConverter* which then determines whether a photon, γ, is accepted as a hit in the DOM and converts it into a PE pulse. The probability of being converted into a hit is given as:

$$P(\gamma \rightarrow hit) = weight_{\gamma} \cdot domAcceptance(\lambda_{\gamma}) \cdot domAngularSensitivity(\theta_{\gamma}) \cdot scalar, \quad (5.1)$$

where the weight of the photon effectively cancel out the domAcceptance as they are the inverse of one another except for a scaling factor as described in 5.1.3. The scalar used is the product between the RDE and the compensation factor from the SPE template. The photon is then saved as a MCPE if the hit probability is higher than a number drawn from a uniform distribution between 0 and 1. In Figure 5.3 this canceling out is more clearly seen. The figure shows a scatter plot of photon wavelength vs. cosine of the zenith angle relative to the DOM. This translates into $cos(\theta_{\gamma}) = 1$ is photons that hit directly in the center of the PMT while $cos(\theta_{\gamma}) = -1$ is photons hitting on top of the DOM. All the photons colored by their probability of being a hit before the hit decision criteria. Furthermore, the DOM wavelength acceptance is on the x-axis and the angular acceptance is on the y-axis. The hit probability clearly follows the angular acceptance

shown on the left. The density of points seem by eye to follow the wavelength acceptance curve.

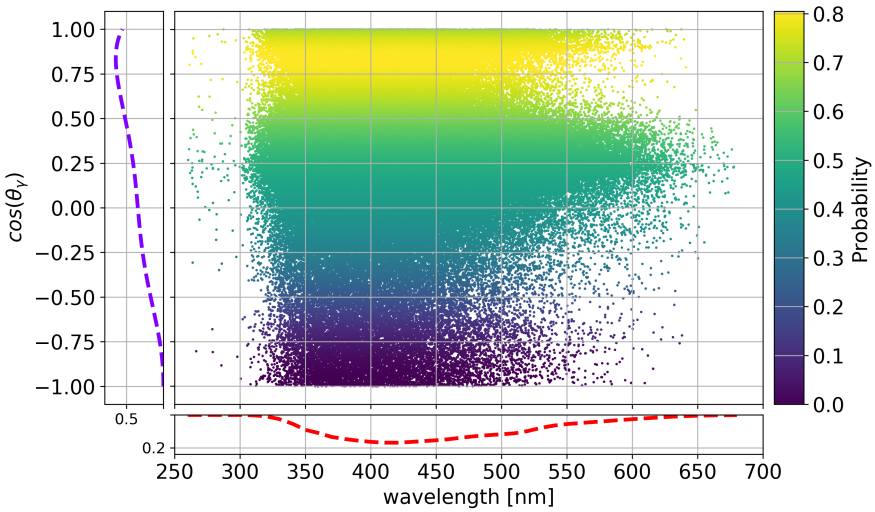

FIGURE 5.3: Scatterplot of photon wavelength vs. cosine of incoming angle relative to the PMT. The color indicates the probability of being a hit from Equation 5.1 . The sideplot on the x-axis has the DOM wavelength acceptance and the sideplot on y-axis the DOM angular sensitivity.

PMT Simulation

The next step is simulating the response of the PMT. This is the first step in the DOMLauncher simulation designed to simulate the electronics of the PMT. The second part of DOMLauncher is responsible for simulating the data read-out from the DOMs. Here the MCPE from the photon conversion is given a charge from a SPE (Single Photo Electron) Charge Distribution. This is a probability density function that describes the charge distributions for each DOM. It is from this distribution the charge given to each MCPE is drawn, hence creating a MC pulse series of times and charges.

Besides simulating the photoelectrons (PEs), PAL (pre-, after-, late-)-pulses are also added in the simulation.

The prepulses are from photons entering the PMT about 30 ns before the normal photoelectron pulses and have a 10-20 times smaller amplitude. The probability of a hit being a prepulse is set to 0.3% along with a time shift of -31.8 ns and a weighted charge of $1/20$ PE.

Afterpulses occur when photoelectrons transversing the PMT ionize residual gas atoms which drift back to the photocathode due to their positive charge. Electrons are then dislodged and pass through the dynode chain. The afterpulse probability is set to 5.9% weighted by the SPE charge distribution. Early afterpulsing is also observed at two peaks $\sim$ 500 and 540 ns from the main peak of the SPE-template. The charge distribution used for early afterpulses is a Gumbel distribution with $\beta = -3.386$ and $\mu = 13.31$. The peak of this charge distribution is approximately 13 SPE equivalents.

Late pulsing occurs when a PE scatters back of the first dynode taking some time to turn back and reach the dynode chain. Late pulses are simulated with a probability of 3.5% with about 4% of that around 25-65 ns, most around 71 ns and approximately 0.2% at 85-160 ns. These are basically single PEs with a time delay and weighted as normal pulses. Everything else is PE pulses with a probability of $1 - P(\text{after pulse}) - P(\text{late pulse}) -$

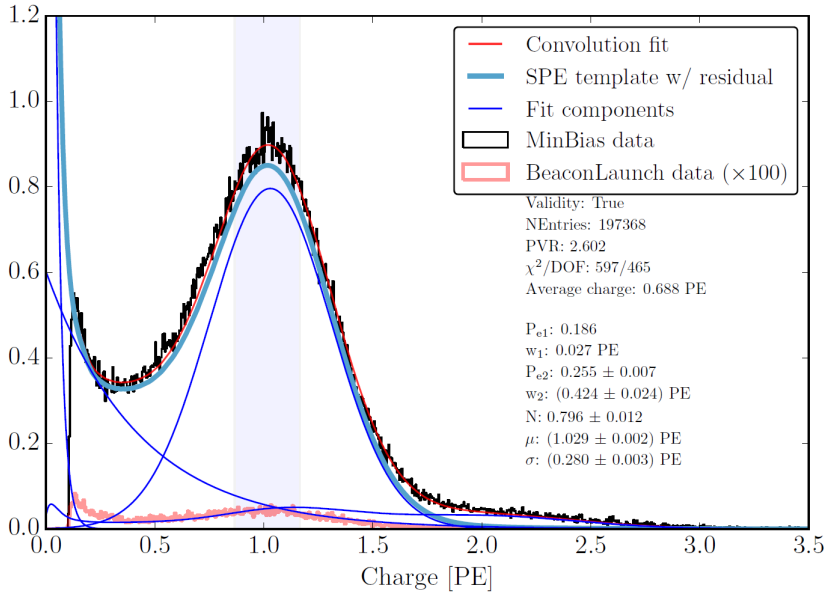

FIGURE 5.4: SPE fit Example from [31].

$P(\text{prepulse}) = 90.3\%$.
The time it takes for a PE to traverse the PMT to the first dynode and for the shower to build up in the dynode chain can vary and is referred to as the "PMT jitter" a time offset of approximately 2 ns is applied using a Gumbel distribution with $\beta = 1.92$ and mean $\mu = 0.15$. An example of a SPE template is shown in Figure 5.4.
Finally some pulse merging is done, even though not being a physical effect, to reduce data size and improve computation time without affecting the physics. Hits within 0.2 ns of each other are merged and weighted to account for all hits merged.

The PMT Simulation fails to reproduce the percentage of pulsetypes expected from the probabilities mentioned above as the distance between the interaction vertex and the hit DOM decreases.

Pulsetype	% received					% expected
Photoelectron	54.58	85.25	87.7	89.26	90.39	90.3
Prepulse	1.32	0.45	0.36	0.32	0.26	0.3
Afterpulse	28.96	9.26	7.64	6.64	6.01	5.9
Late pulse	15.15	5.04	4.3	3.79	3.32	3.5
Distance from vertex	6.78 m	12.07 m	18.53 m	25.29 m	51.33 m	

TABLE 5.1: Table with the distribution of pulse types in DOMs at different distances from the interaction vertex from the PMT simulation. At distances from $\sim$ 25 m and further the distribution of pulses starts to resemble the expected values.

In Table 5.1 the percentage of the pulse type received by a DOM at different distances from the interaction vertex is shown. At some distance the photons and PEs start to saturate the PMT. This indicates a caveat of the 50 GeV e^- being simulated to close to a DOM. The percentages converge to what is expected at distances $\sim$ 25 m and more, while at closer distances it is clear that the amount of PEs dramatically falls off between $\sim$ 12 and $\sim$ 6 meters. At the closest distance an excess of 1% prepulses, 12% late pulses and 22%

after pulses is received by the DOM.

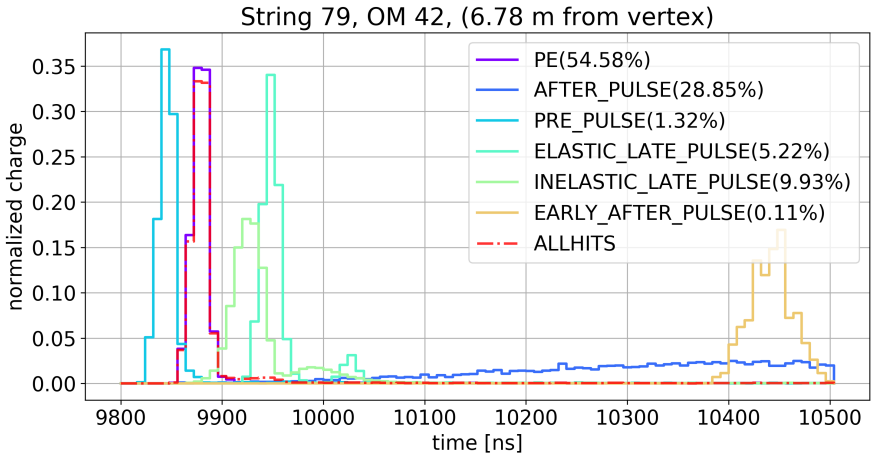

FIGURE 5.5: The normalized charge vs. time distribution of the pulse types received by DOM 42 on string 79, located 6.78 m from the interaction vertex. The excess of late pulses cause a minor distribution at 9950 ns in the tail of the red dashed line. The red dashed line shows the combined distribution of weighted pulses received by the DOM.

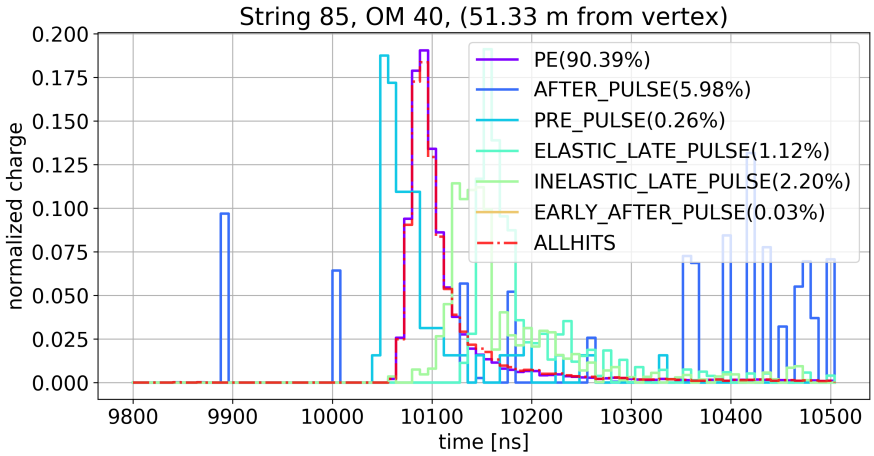

FIGURE 5.6:]
The normalized charge vs. time distribution of the pulse types received by DOM 40 on string 85 located 51.33 m from the interaction vertex. The red dotted line shows the combined distribution of weighted pulses received by the DOM which follows the PE pulse types (purple line).

In Figure 5.5 histograms of the time distribution of the pulse types weighted by charge at a distance of 6.78 m corresponding to the column with the minimum distance in Table 5.1 is shown. The red dashed line in Figure 5.5 is the weighted charge vs. time distribution of all collected pulses. Around 9950 ns there is a small distribution from the excess of late pulses whilst the excess of pre- and afterpulses doesn't show irregularities in the weighted combined distribution by eye but intensive zooming will show a small rise in the afterpulse area of the tail. This is an artefact from the normalization of the individual histograms and the normalization of the combined histograms. Comparing this to Figure 5.6 that corresponds to the column with the maximal distance it is clear that the small distribution of afterpulses in the tail of the collected pulses has vanished along with the

excess of latepulses. Early afterpulses are almost non existing while afterpulses unexpectedly appear at earlier times than the PE and latepulses. The charge distributions

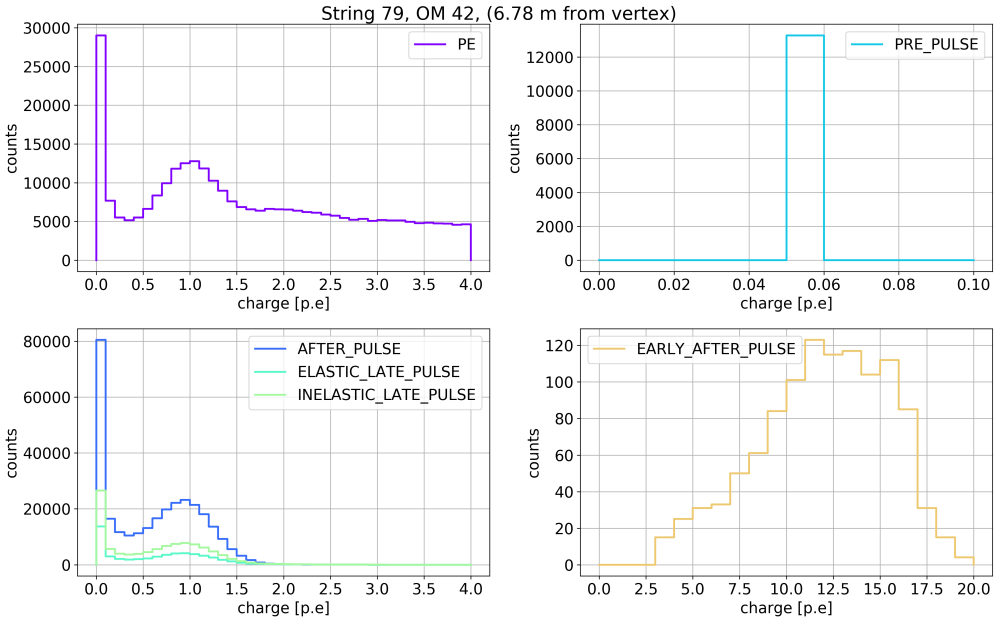

FIGURE 5.7: Charge distributions of the different pulse types in a DOM, close to the interaction vertex, from the PMT simulation. The distribution of the PE pulses in the top left plot deviates from the expected SPE template distribution. The tail isn't flattening out as fast as expected but extends to higher charges. The pre-pulses, afterpulses and late pulses all have the expected distribution, though having a larger count than expected.

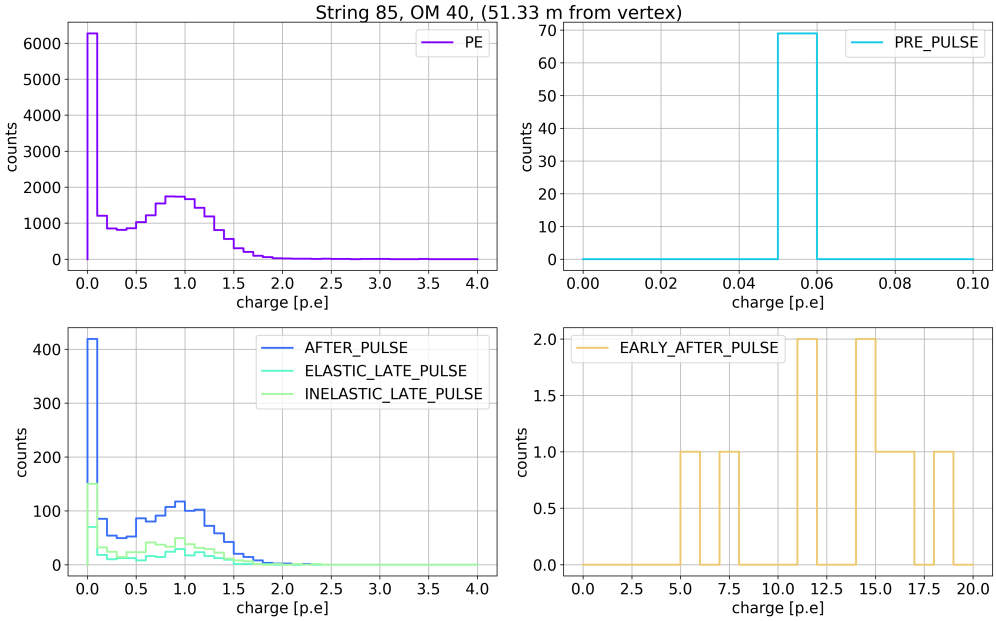

FIGURE 5.8: Charge distributions of the different pulse types in a DOM, far from the interaction vertex, from the PMT simulation. The distribution of the PE pulses in the top left plot follows the expected SPE template distribution. The pre-pulses, afterpulses and late pulses all have the expected distribution and count as well.

for the pulse types in the two DOMs are shown in Figures 5.7 and 5.8. In both cases the late- and afterpulses follow the SPE charge distribution, the early afterpulses follow the Gumbel distribution mentioned above (though difficult to see for the DOM at 51.33 m from the interaction vertex due to low statistics at greater distances) and the prepulses have a charge of $1/20 = 0.05$ PE, all as expected. The width of the prepulses is a binning artefact as the charge for this pulsetype is a constant. When comparing the regular PE pulses in the top left of the figures, the distribution from the DOM close to the interaction vertex deviates from the expected charge distribution. Instead of falling off after the peak at 1.0 PE, the DOM receives many pulses with a charge above 1 PE. In the DOM further away the PE distribution exactly follows the SPE charge distribution. Further investigation into what is causing this issue in DOMs close to the interaction vertex has been out of scope for this thesis, but a clear incentive to pursue this in the future is given here. A natural starting point would be to dig into the pulse merging algorithm and the saturation parameter in the PMT simulation module.

DOMLauncher

The DOMLauncher module is responsible for simulating the raw detector response. By using the weighted pulses given by the PMT simulation, it transforms the pulses based on discriminator thresholds, LC conditions and fills the FADC and the ATWD waveforms. When developing the SPE templates a disagreement between data and MC was found below 0.25 PE. The discriminator threshold is the set to trigger at this value to obtain a better data/MC agreement.

5.1.5 Level 1 and 2

The triggering and filtering steps of the simulation are beyond the scope of this work and will not be described in detail. On the short side, these steps do event selection based on a numerous amount of criteria, from boundaries on parameters to uncertainty in the FADC and ATWD readouts.

Chapter 6

Analysis

When trying to advance the reconstruction methods of low energy particles, the first step in this work is to test how the Millipede module described in Section 4.1 behaves at low level, before testing an actual reconstruction of events. The testing at low level is done by extracting hypotheses from Millipede given the simulated data described in Section 5.1 where the same 50 GeV e^- cascade was simulated 10 000 times. The reasoning behind simulating an electron and not a neutrino (since it is neutrinos we wish to reconstruct) stems from the fact that we only reconstruct the light emission from the products of neutrino interactions in the ice. In general we reconstruct a combination of cascades and tracks, but for this work we ignore tracks and focus on cascades in the detector. This is valid for ν_e and ν_τ CC interactions and all NC events. Currently, in IceCube, it is not possible to distinguish between EM and hadronic cascades, so this is simply represented as a EM cascade in the simulation used in the work.

6.1 Testing the Millipede Hypothesis

When re-simulating the same event multiple times effectively canceling out the statistical randomness from single events makes it possible to test and analyse the average behavior of the hypotheses generated in Millipede. Millipede takes the input data from each event in terms of a series of pulses in each DOM. This is then binned in Millipede and minimizer is searching the likelihood landscape for an optimal hypothesis given the event data. The minimizer is given a seed which is a first guess for the attributes of the particle being reconstructed (think of it as a starting point in the likelihood landscape).

This low level testing is done by extracting the hypothesis using the true particle attributes as the seed and not doing any minimizing. This means that it is possible to compare the optimal scenario hypothesis and compare it to the truth (input data waveform). The data and the hypothesis waveforms are averaged over all the events and compared. The average of the MC data cancels out statistical randomness and is why the average behavior is analyzed opposed to event-by-event comparison. DOM 37 on string 79 has been selected as an example in this work showing a representative picture of all the DOMs. The binning used has a binwidth of 8 ns in a range from 9800 ns to 10500 ns. Figure 6.1 shows the comparison between averaged MC data and averaged hypotheses along with the ratio between the averaged MC data and averaged hypotheses. On average the hypotheses underestimates the amount of charge in each bin and many fluctuations are seen in the ratio plot from bin to bin. The fall off after the main peak also shows a mismatch in timing between the hypothesis and MC data. It is the assumption when using DirectReco that effects from PMT simulation and noise effectively will cancel out. This is not the case here and changing around parameters in *Millipede* doesn't make the hypothesis match better with the MC data.

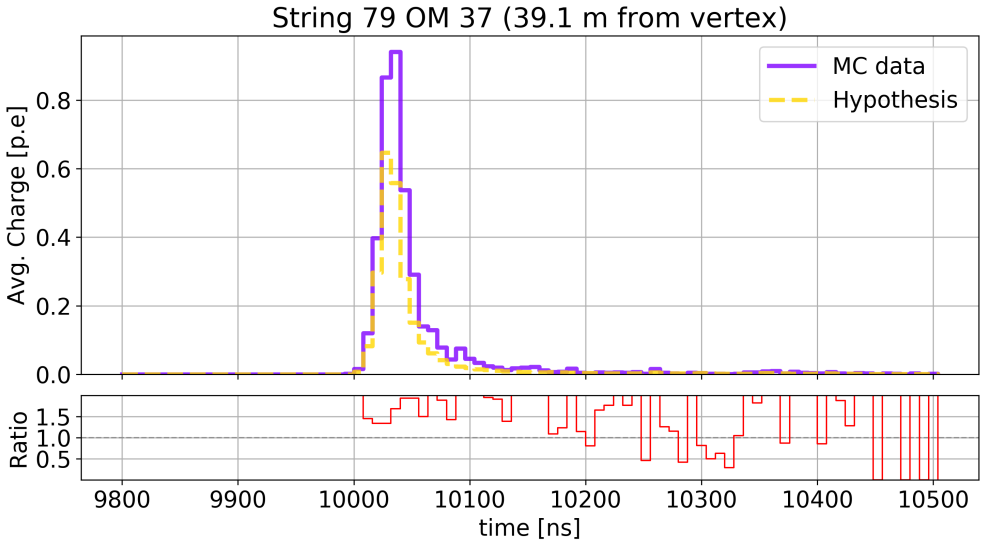

FIGURE 6.1: Plot of the average charge vs. time waveform using uniform time binning. Purple line is the average MC data using detector simulation. Yellow dashed line shows the average hypothesis extracted from *Millipede* at the truth seed. Red line is the ratio MC data/Hypothesis.

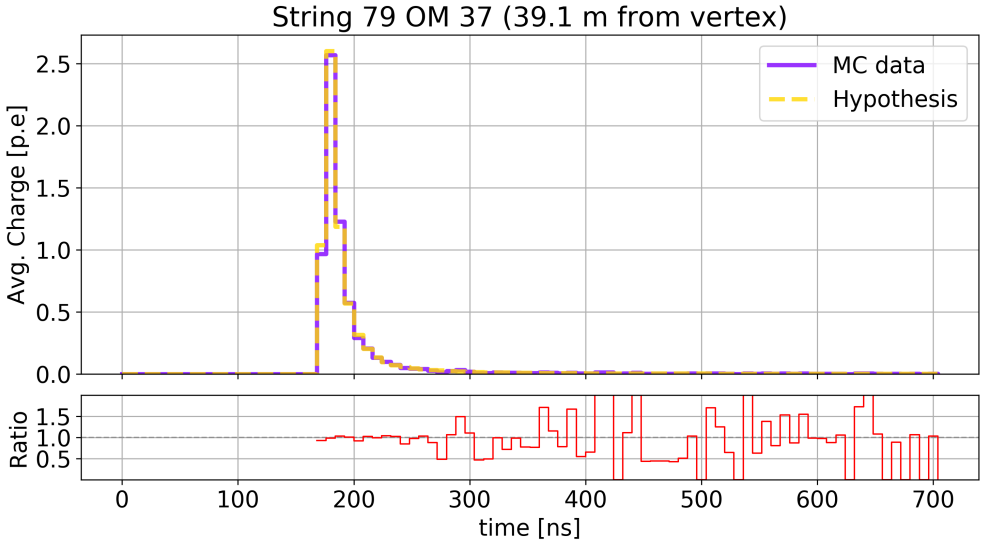

FIGURE 6.2: Plot of the average charge vs. time waveform using uniform time binning. Purple line is the average MC data using no detector simulation. Yellow dashed line shows the average hypothesis extracted from *Millipede* at the truth seed. Red line is the ratio MC data/Hypothesis.

By removing noise, PMT simulation, and DOMlauncher from step 3 of the simulation along with the level 1 and 2 filtering and triggering makes it possible to test the hypotheses against MC data at an even lower level of simulation. A module that converts at photon hit, on a DOM, 1-to-1 to a MCPE, effectively meaning that each and every photon gets a charge of exactly 1 PE, is instead used in step 3. When extracting the hypothesis,

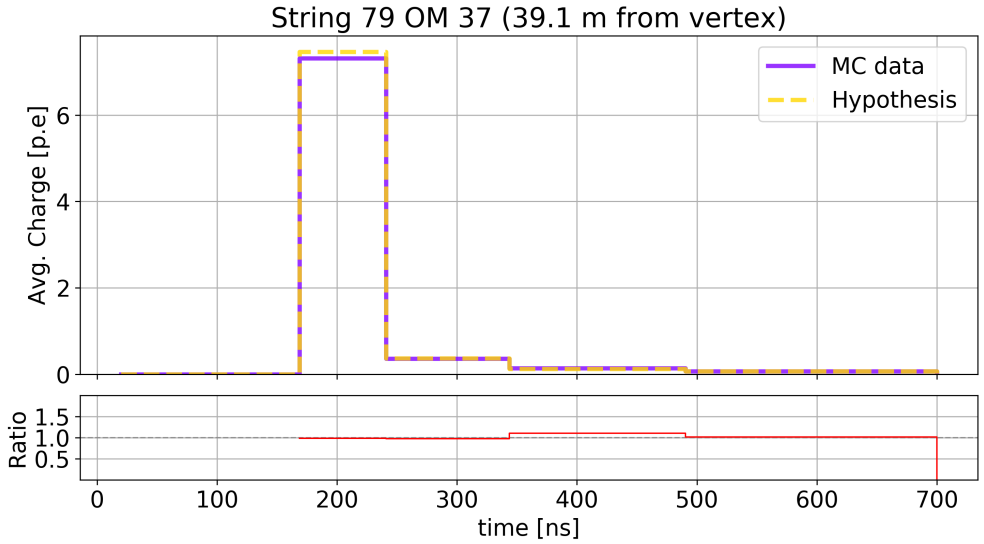

FIGURE 6.3: Plot of the average charge vs. time waveform using logarithmic time binning. Purple line is the average MC data using no detector simulation. Yellow dashed line shows the average hypothesis extracted from *Millipede* at the truth seed. Red line is the ratio MC data/Hypothesis.

the expected charge in each bin needs to be scaled accordingly by RDE and the compensation factor, described in Section 5.1.3, to make up for the excess of light simulated in *CLSim*. In Figure 6.2 is a comparison of the averaged hypotheses from Millipede and MC Data when the is no detector simulation. A clear improvement is seen especially at the rise and main part of the waveform that almost matches perfectly when looking at the ratio. The tail of the distribution still shows many fluctuations which could be an issue when summing up the charge in all DOMs. The shift in time on the x-axis is an artefact of removing any trigger time from the simulation and the time starts at zero when the simulated e^- appears in the detector. The binning has just been shifted from 9800-10500 ns to 0-700 ns. In the master thesis by Thomas Halberg [32], issues concerning time binning methods in Millipede was found. This leads to exploring a different binning method than what is currently available in Millipede. The Millipede hypothesis and MC data is ultimately a set of charge vs. time histograms. In DirectReco oversampling is used where the event is resimulated N times and averaged. Using low oversampling (N) results in limited statistics in each bin of the hypothesis which in turn can create statistical fluctuations in the likelihood landscape, complicating things for the minimizer. Limited statistics in the bins can be avoided by using larger bins. Using a logarithmic binning gives smaller bins in the beginning of the readout window where most photons are detected, and larger bins in the tail where less photons are detected. The smaller bins in the beginning of the readout window also conserves some time information about the event. An algorithm providing logarithmic binning has therefore been added in Millipede [‡]. In Figure 6.3 is the comparison of averaged MC data and averaged Millipede hypothesis using logarithmic binning. Using the logarithmic binning make the hypothesis almost perfectly match up with the MC data. All in all this shows that the assumption of PMT simulation and noise effectively cancel out in DirectReco isn't true. Only when removing noise and the detector from the simulation, it is possible to make the optimal hypothesis from Millepede to match the MC data. Using logarithmic binning prevents low statistics

[‡]For now hardcoded but definitely possible to make this a persistent option.

in bins at lower oversampling while maintaining the time information.
The next step in the analysis will be examining how the likelihood landscape behaves at different values of oversampling, to create a smooth likelihood landscape, minimizing fluctuations creating local minima, that potentially gets the minimizer stuck.

6.2 Choosing Oversampling

The reconstruction of the energy in low energy events is an issue in DirectReco. The following sections will therefore use the energy likelihood landscape as a measure for deciding on which oversampling to use when moving on to run a full reconstruction. The likelihood landscape in energy is studied using the no detector simulation using uniform time binning and logarithmic binning at oversampling values 100 and 1000.

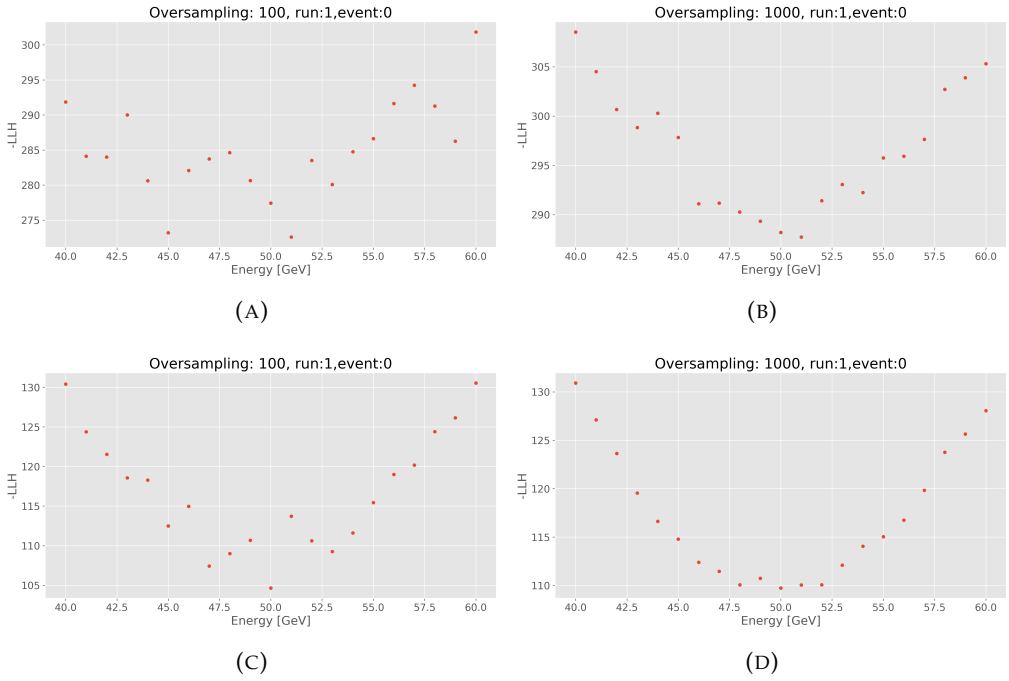

FIGURE 6.4: The log likelihood landscape in energy for event 0. All other parameters are fixed at truth and energy is scanned from 40-60 GeV in steps of 1 GeV. (A) and (B) Energy LLH landscape at respectively oversampling 100 and 1000 using uniform binning. (C) and (D) Energy LLH landscape at respectively oversampling 100 and 1000 using logarithmic binning

Fig 6.4 shows the LLH landscape at different binning methods and oversamplings. The top row, **(A)** and **(B)**, show the scans using uniform time binning at oversampling 100 and 1000 respectively. At oversampling 100 the fluctuations in the LLH landscape are dominating and a clear global minimum at the truth of 50 GeV isn't present. Going to oversampling 1000 in **(B)** smoothens out the fluctuations seen in **(A)**. A more clear minimum around 50 GeV is present but there are still fluctuations creating local minima. The bottom row **(C)** and **(D)** show the scans using the logarithmic binning method. A clear improvement is seen from uniform time binning and when moving to oversampling 1000 in **(D)** the energy LLH landscape seems smooth around the global minimum compared

to uniform time binning at the same oversampling. This again confirms the choice of logarithmic binning while an oversampling of 1000 is chosen for further analysis.

6.3 The Ever Changing Loglikelihood Energy Landscape

The loglikelihood landscape in energy in a perfect scenario should have a parabolic shape with a minimum at the true energy. Exploring the landscape, however, shows an inconvenient truth. The energy landscape tells a much different story, when scanning it at reconstructed parameter values, rather than scanning at the truth. To be able to make a likelihood scan at the reconstructed parameters it is necessary to run a quick reconstruction of the 50 GeV e^- no detector simulation. When reconstructing using real data it is not possible to used the truth as seeding. Instead of using the truth as the seed a more realistic scenario seeding is chosen. The seeding for the position of the interaction vertex center of gravity (COG) is used. The COG is defined as the mean position of photons that hit DOMs, weighted by the charge received by the DOMs. For the directional seeding a line-fit is performed and then used as a seed in a single photon electron reconstruction (SPE-fit). The line-fit produces an initial track based on the hit times and locations of the hit PMTs using a least squares minimization. The SPE-fit uses the line-fit and the event data in a likelihood maximization algorithm to reconstruct an estimate of the zenith and azimuth angle. The energy seed is specialized for the 50 GeV event by multiplying the total amount of pulses recorded in the event with a factor only usable for the 50 GeV event. The oversampling has been set to 1000, the minimizer tolerance to 0.01 and the step size in energy is set to 2 GeV with everything else kept at default.

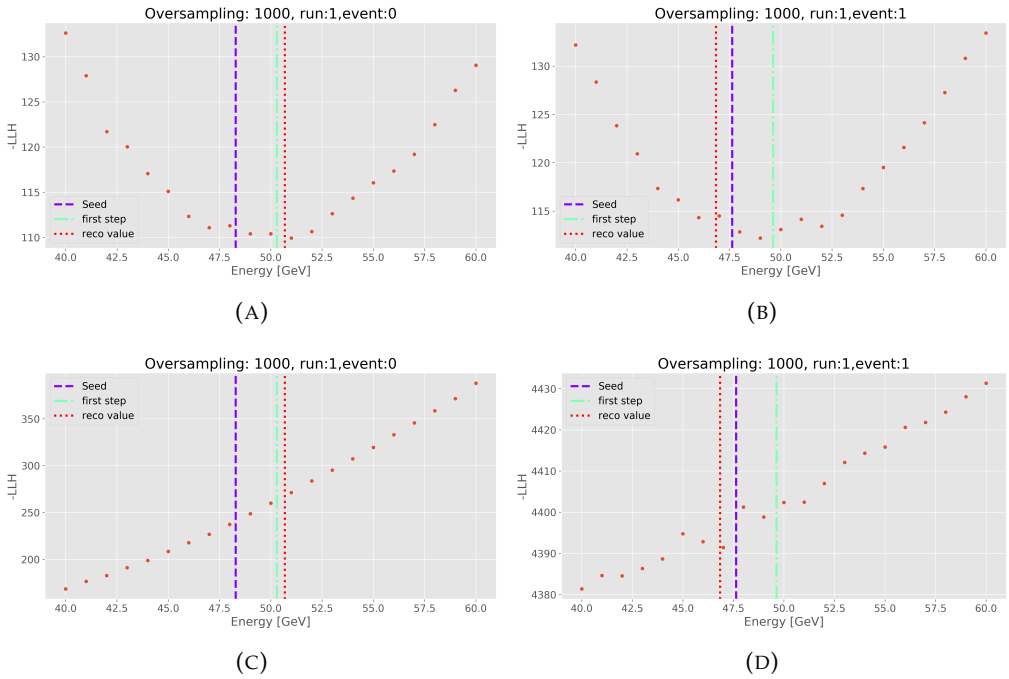

FIGURE 6.5: **(A)** and **(B)** show the LLH space in energy extracted at the true parameters for event 0 and 1 respectively. **(C)** and **(D)** show the LLH space in energy extracted at the reconstructed parameters for event 0 and 1 respectively. The purple line is the seed value, the green line is the first step of the minimizer and the red line is the reconstructed value.

Fig 6.5 shows the scans of the energy loglikelihood landscape. Top row **(A)** and **(B)** show event 0 and event 1 from the simulation respectively. Here the energy landscape is scanned while fixing all other parameters at the true values. Bottom row **(C)** and **(D)** show the same scans extracted at the reconstructed parameters of the respective events. In each plot the purple dashed line is the seeded value, the green line is the first step of the minimizer under the assumption that it always takes the first step towards higher energy [§] and the red line is the reconstructed value. For event 0 the reconstructed value is closer to the true value compared to the seed while the opposite is true for event 1. In either case the log likelihood landscape changes from a parabolic shape to almost straight line shape. From the scans one would expect the minimizer to perform worse than what is actually happening. The minimizer in **(D)** seems to get stuck in a local minimum at $\sim$ 47 GeV where as in **(C)** the minimizer would be expected to move to an energy value even yet lower. The scale of the negative log likelihood value on the y-axis is about 10 GeV per scan point which means that an even finer scan could reveal large fluctuations and local minima here as well. The scale in **(D)** is only a few GeV per scan point even though at much higher values than in any of **(A)**, **(B)** and **(C)**.
This is an interesting, however not promising, feature in the loglikelihood landscape. The 50 GeV e^- simulated here has shown unexpected features mentioned in Section 5.1.4 and it is unsure whether this feature in the likelihood landscape is a consequence of an unfortunate choice of interacting vertex in the simulation. From here moving to a full reconstruction with a more realistic simulation needs to be done. This is to see how well DirectReco is at reconstructing events after removing parts of the simulation and changing the binning. The same likelihood scans can then be done on a more realistically simulated scenario.

6.4 Running A Full Reconstruction

To run the full reconstruction a new simulation is made to reflect a more physical scenario. The no detector simulation described in Section 6.1 is used but instead of simulating the same event over and over again, a distribution is chosen for each parameter. One thousand e^- are simulated over a uniform energy range of 10-50 GeV. The interaction x and y vertices are placed within 33 meters of String 36 and the z vertex is simulated in a range from -230 to -430 meters which is inside the DeepCore region of the detector. The distribution in azimuth is uniform from 0 to 2π while only simulating upgoing electrons in the detector using a uniform distribution in $cos(\theta_{zenith})$ from -1 to 0.
The seeding used is COG for x,y,z and a linefit with an SPE fit for direction in azimuth (ϕ) while time and zenith angle (θ) have been chosen to be fixed at the truth. By fixing time at the truth, it is ensured that it doesn't seed at late enough times to be in a somewhat flat part of the likelihood landscape and can't be recovered by the reconstruction.

The zenith angle reconstruction is having problems reconstructing unimodally to the truth. Figure 6.6a shows the zenith reconstruction performance when only fixing time to truth. The performance shows two separate distributions. One centered around 0 as expected and a bias centered around -1.6 which is approximately $-\pi/2$. This bias is most likely caused by more horizontal events with $\theta_{true} \sim \pi/2$ reconstructing as downgoing with $\theta_{reco} = 0$, which is unwanted since only upgoing events are simulated. Figure 6.6b shows a scatter plot of the ratio $\frac{|\theta_{reco}-\theta_{true}|}{|\theta_{seed}-\theta_{true}|}$ vs. θ_{true}. The ratio is a measure of how the reconstruction performs against the seed as a function of the true value. Points below the dashed 1.0 line on the y-axis mean that the events reconstruct closer to the truth than the

[§]The simplex algorithm used in the minimization process, uses the initial seed point and the first step value to evaluate which direction to move from here.

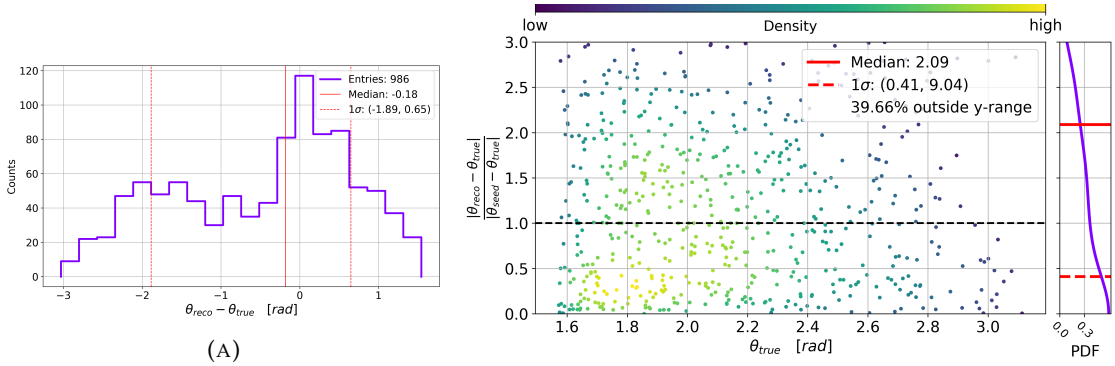

(A) (B)

FIGURE 6.6: **(A)** Reconstruction performance for the zenith angle when fixing the time parameter at truth. **(B)** Performance of the ratio between reconstruction and seed of zenith against the truth. In both plots the red line shows the median and the dashed red lines are the 1σ on either side of the median.

initial seed. A PDF of the density of the ratio points is shown on the right. The majority of the events reconstruct worse than the initial seed and the scaling on the y-axis cuts off almost 40% of the points which lie above a ratio value of 3. Turning to the x-axis with θ_{true} there is a clear bias, where upgoing events reconstruct better than horizontal events which confirms the $-\pi/2$ bias in Figure 6.6a. The focus in this work is on improving the energy reconstruction that has caused issues in DirectReco at low energies which along the above issue leads to running a reconstruction where fixing both the time and zenith angle to the truth applies [32].

6.4.1 The Reconstruction

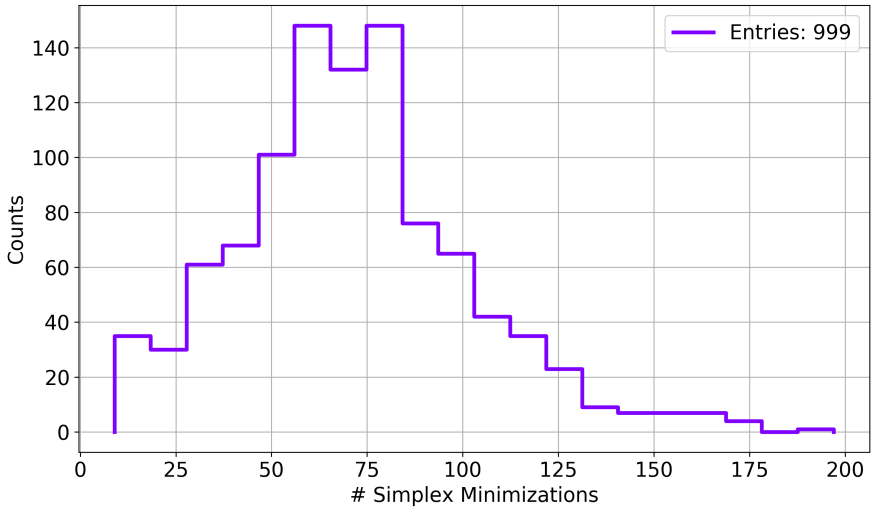

FIGURE 6.7: Unimodal distribution of the amount of simplex minimizations pr event in the reconstruction.

Studies done using the no detector simulation mentioned in Section 6.1 show a bi-modal distribution in the number of minimizations done in *Millipede* where the events with a low amount of minimizations perform worse than the distribution with a larger amount. This is also seen in studies done by fellow MSC. student at NBI, Jonathan Jegstrup, using the D-Egg, a DOM type, with an up-facing and down-facing 8" PMT, that will be used in the IceCube Upgrade [33].

In this study the no detector simulation for testing the Millipede hypothesis also showed unexpected behavior when analysing the simulation in Section 5.1. The 50 GeV e^- in that simulation was unfortunately placed nearby and pointing almost directly into a DOM thereby shadowing other DOMs that otherwise would have received light as seen in Figure 5.1. Using the simulation with a more realistic scenario strongly reduces this caveat and the distribution of minimizations pr. event follow a uni-modal distribution as expected and is seen in Figure 6.7. All performance plots of position and azimuth reconstruction can been seen in Appendix A.

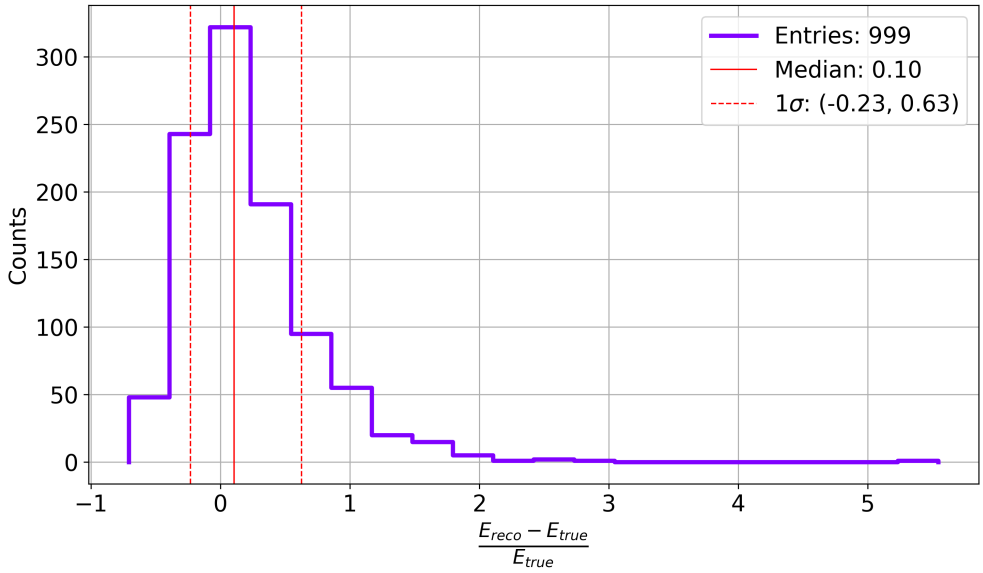

FIGURE 6.8: The performance of energy reconstruction in terms of the fractional error. The distribution is show in purple. The red line is the median and the dashed red lines show the $\pm 1\sigma$ from the median.

The performance of the energy reconstruction is shown in Figure 6.8. The distribution of the fractional error has a peak around zero and features a long tail, with a bias towards an overestimate of the energy. Energy overestimates from 100-550% (!!!) are seen. The median (red line) is 0.1 so within 10% of to optimal value at zero. The accuracy is of more concern with a 1σ width of 85% combined with the majority of 62% higher than the median. If the bias in the tail could be eliminated the performance in energy would look somewhat promising.

By comparing the fractional error on the energy reconstruction against the fractional error on the energy seed it is possible to get an idea of how the reconstruction performs when seeding on either side of the true energy seen in Figure 6.9.

If a scatter point is on the grey 1:1 line, means that hasn't moved away from the seed at all. More interesting is the bias that almost all events reconstruct to a higher value than the seed. Only few shift to lower values. Another feature exposed in this plot is the bias at seeding lower than the truth. Here the reconstruction is still higher than the seed but the

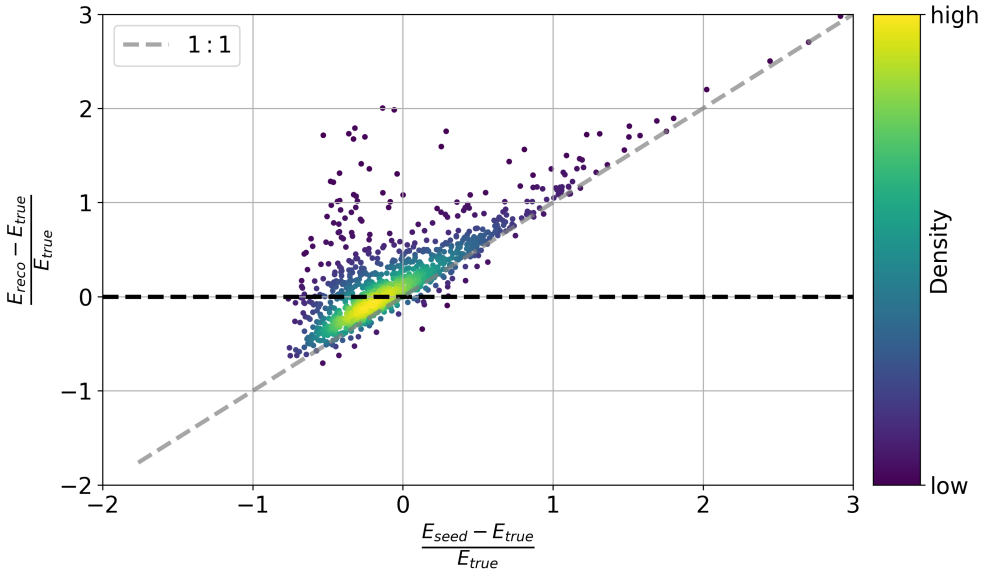

FIGURE 6.9: Scatterplot of the fractional error on the reconstructed values vs. the fractional error on the seeded values. The grey dashed line is the 1 : 1 line where the fractional errors match.

minimizer seems to be exploring a wider range of the likelihood landscape, compared to all points above zero on the x-axis, where the minimizer only explores a range somewhat closer to the seeding. The optimal scenario would show the points centering on the black horizontal line where the fractional error on the reconstruction is zero. This illuminates the possibility of the minimizer not performing optimal. The simplex is known to take its first step towards higher energies, making it a possibility that it gets stuck in small local minima and why Figure 6.9 shows a tendency to reconstruct at higher values than the seed no matter if the seed is lower or higher than the truth.

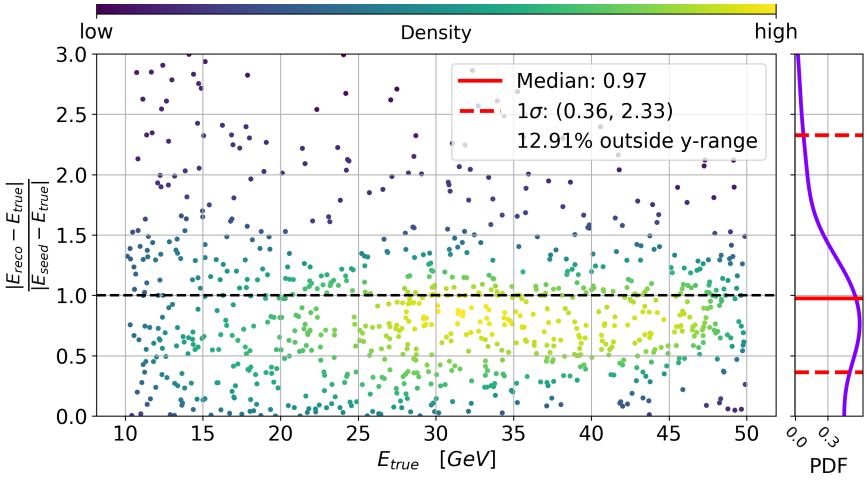

FIGURE 6.10: Scatterplot of the ratio of the reconstruction and seed performance vs. true energy. Events below the black dashed line reconstructs closer to the truth than the seeded energy and vice versa. On the right the distribution of the ratio is shown.

By analysing the ratio $\frac{|E_{reco} - E_{true}|}{|E_{seed} - E_{true}|}$ against the true energy it's is possible to see if there

would be any bias of the reconstruction doing better than the seeding at certain energies. A ratio below one, means that the reconstruction has moved closer to the true value compared to the seed. We want the reconstruction to do a better job than the seed otherwise the entire reconstruction would be purposeless. In Figure 6.10 the ratio is plotted against the true energy for each event. The right plot of the figure shows a PDF of the distribution of the ratio points. The optimal scenario would have the entire distribution beneath the 1.0 line which is not the case. Because of scaling on the y-axis, about 13% of the ratio points lie above 3.0 and are not seen in the plot. The median (red line) and the width (red dashed lines) are calculated using the entire distribution. The median is below 1 but only slightly at 0.95. This means that just above 50% of events reconstruct to a value better than the initial seed, which is terrible when trying to obtain a reasonable resolution in the reconstruction. This leads back to this most likely being an minimizer issue with the minimizer mainly moving towards better reconstruction when seeded at values lower than truth. There is also a higher density of events reconstructing slightly better than the seed between 30-50 GeV.

The Return Of The Ever Changing Likelihood Landscape

Once again likelihood scans in energy are performed fixing all other parameters at the truth and at the reconstructed values only this time for the reconstruction using the more realistic simulation.

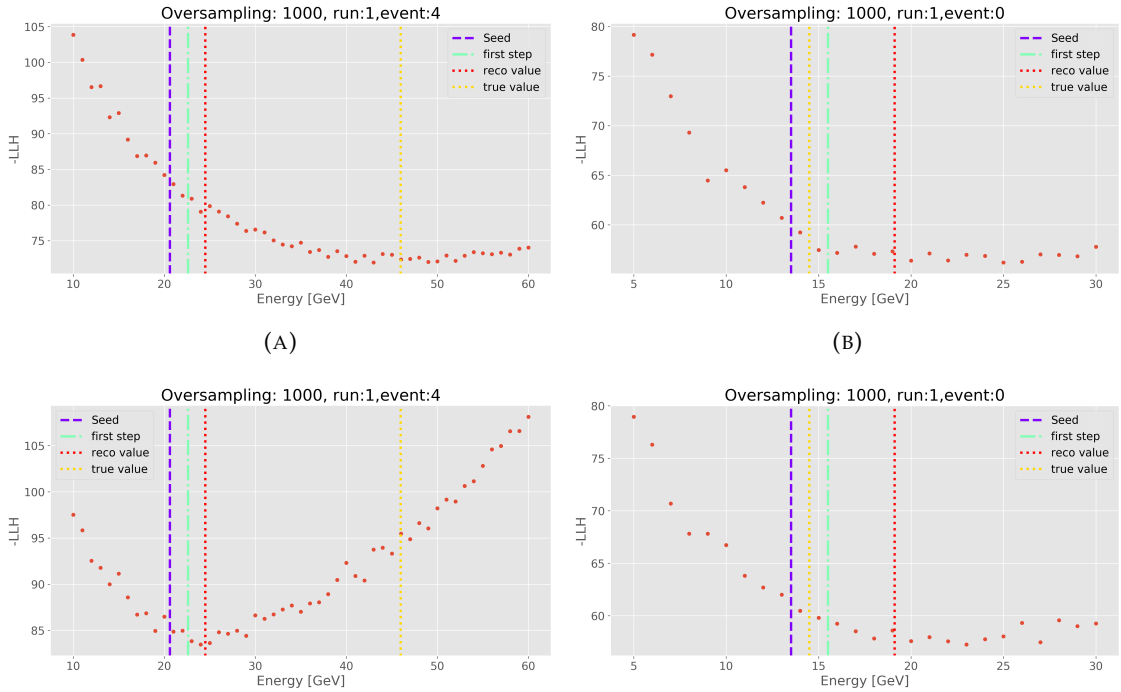

FIGURE 6.11: **(A)** and **(B)** show the LLH space in energy extracted at the true parameters for event 4 and 0 respectively. **(C)** and **(D)** show the LLH space in energy extracted at the reconstructed parameters for event 4 and 0 respectively. The purple line is the seed value, the green line is the first step of the minimizer. The red line is the reconstructed value and the yellow line is place at the true enegy of the event

The scans are done on event 4 and 0 and are shown in Figure 6.11. For event 4 the reconstruction is doing better than the seed with $\frac{|E_{reco}-E_{true}|}{|E_{seed}-E_{true}|} = 0.85$ and for event 0 the reconstruction is doing mush worse with $\frac{|E_{reco}-E_{true}|}{|E_{seed}-E_{true}|} = 4.71$. The left column plots **(A)** and **(C)** show event 4 that has a high true energy of 46 GeV. **(A)** is scanned at the truth and shows a wide global minimum around the true value whereas the reconstructed value seem to be stuck in a local minimum at 24 GeV even though making it's way from the seed towards the global minimum. When comparing to **(C)** that is the same event but scanned at the reconstructed value it is clear that the minimizer believes that it has found the global minimum. Unfortunately the minimum is almost 50% away from the truth. The minimum in **(A)** has a lower -LLH value than the minimum in **(C)** and could have possibly been found assuming the minimizer had been exploring a wider range of the likelihood landscape. The right column plots **(B)** and **(D)** show event 0 which has a true energy of 14.5 GeV. Here the landscapes, when scanning at the truth **(B)** and at the reconstructed values **(D)**, are very similar. The global minimum is at higher energy than the actual truth and even though the seed is very close to the truth, it moves past the truth at the first step, and the minimizer reconstructs at the start of the global minimum. Again the issues concerning low energy reconstruction is in non smooth likelihood landscapes that has global minimums that isn't near the truth along with a minimizer having trouble navigating the energy likelihood landscape. On the positive side, the other parameters x,y,z and azimuth looks predominantly good, especially the z vertex.

6.4.2 Z Performance

In this section the performance of the z vertex reconstruction is analyzed. This is from the same reconstruction used above when analysing the energy performance.

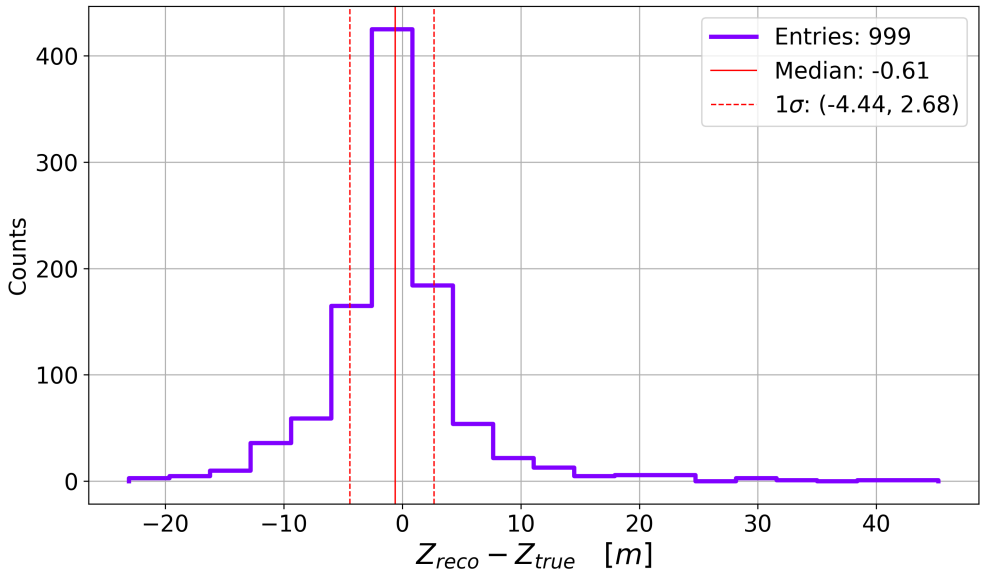

FIGURE 6.12: The performance of reconstruction of the Z vertex. The distribution is show in purple. The red line is the median and the dashed red lines show the $\pm 1\sigma$ from the median.

The performance in z stands in sharp contrast to the energy reconstruction performance. Figure 6.12 shows the performance of the z reconstruction. The distribution of $Z_{reco} - Z_{true}$ nicely centers around 0, with a median of -0.61. This tells us that on average the z

vertex reconstructs a mere 61 cm too low. The total width is 7.12 meters with a slight bias towards reconstructing a but lower than the truth.

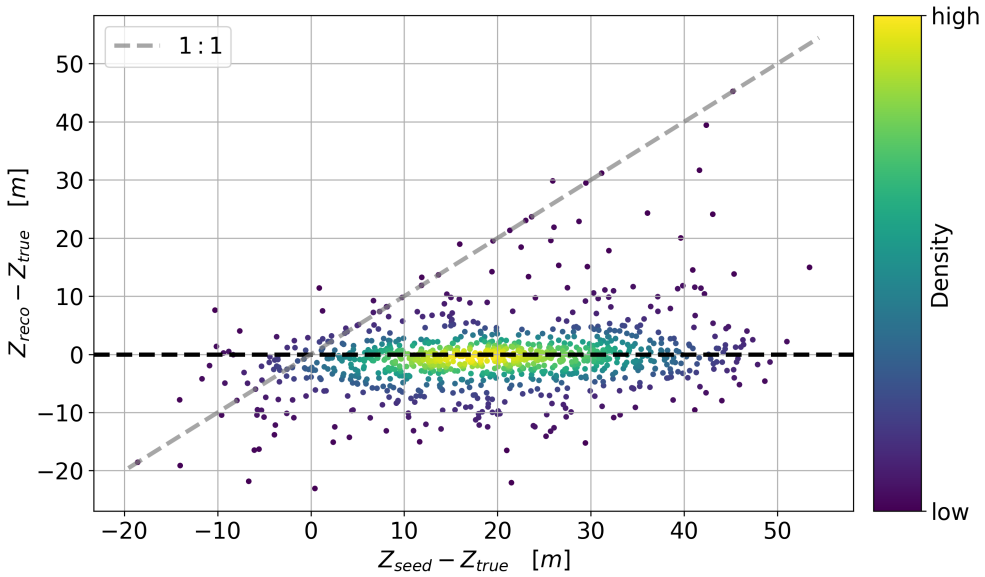

FIGURE 6.13: Scatterplot of the error on the reconstructed values vs. the error on the seeded values. The grey dashed line is the 1 : 1 line where the errors match.

When analysing at the scatter plot in Figure 6.13 showing the reconstruction error vs. the seed error, the reconstruction performs amazingly independent of the seed error. The vast majority of scatter points end up on and nearby the horizontal black dashed line that signifies zero error on the reconstruction. No matter the error on the seed, the minimizer seem to be able to reconstruct a value reminiscent of the truth.

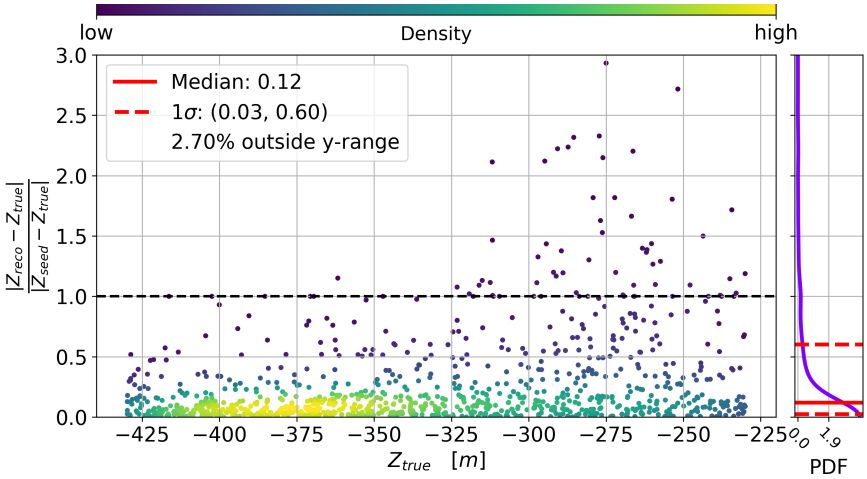

FIGURE 6.14: Scatterplot of the ratio of the absolute distance between the reconstructed energy and truth and the absolute distance between seed and truth vs. true energy. Events below the black dashed line reconstructs closer to the truth than the seeded energy and vice versa. On the right the distribution of the ratio is shown.

Figure 6.14 show the absolute error ratio between the reconstruction and the seed and a

function of the truth. This is almost an optimal scenario. The PDF on the right hand side plot shows the distribution of the points where only 2.7% is outside the y-range. With a median of 0.12 and a σ_+ of 0.6 tells us that $\sim$ 84% of the points reconstruct 40% or more closer to the truth compared to the seed and 50% reconstructs 88% or more closer to the truth. The density reveals a bias when the truth is in the bottom of DeepCore. Here the minimizer is reconstructing better than the seed compared to above -325 meters.

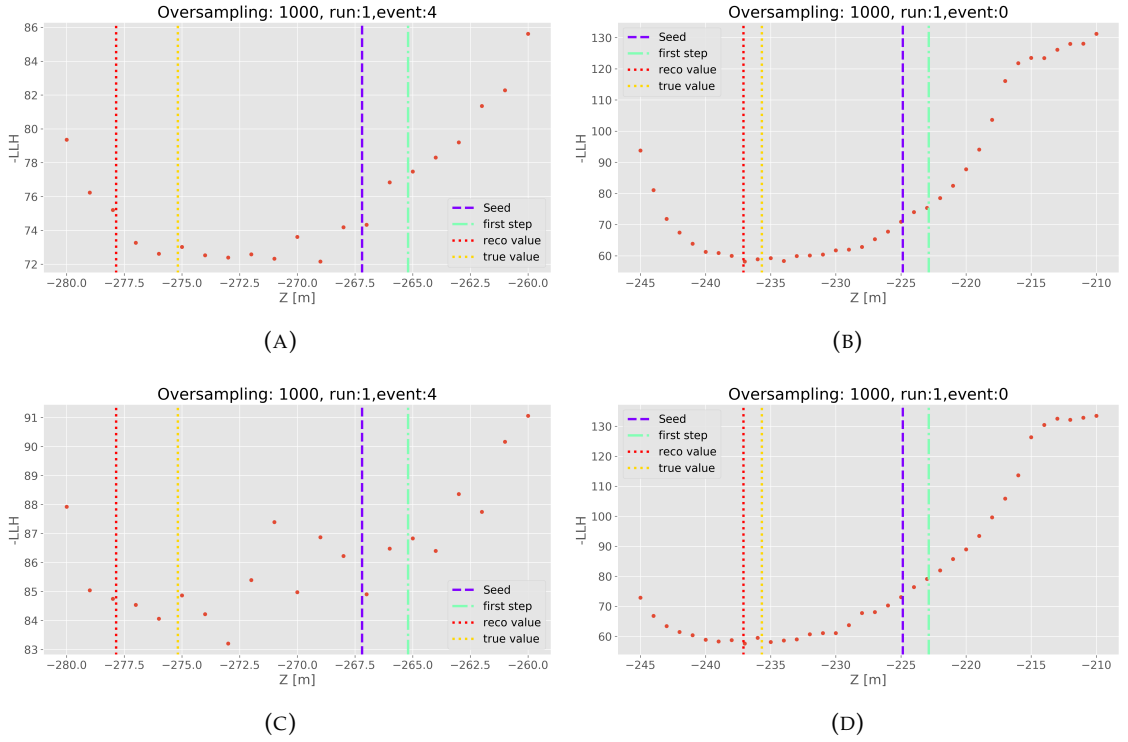

FIGURE 6.15: **(A)** and **(B)** show the LLH space in energy extracted at the true parameters for event 0 and 1 respectively. **(C)** and **(D)** show the LLH space in energy extracted at the reeconstructed parameters for event 0 and 1 respectively. The purple line is the seed value, the green line is the first step of the minimizer and the red line is the reconstructed value.

A visualization of the likelihood landscape in z using the true and the reconstructed values, of the other parameters, respectively is shown in Figure 6.15. The plots shows the same events that was used in the energy analysis, event 4 and event 0. In energy event 4 had better reconstruction than the seed and event 0 had a worse reconstruction than the seed. In z, event 4 has a ratio of $\frac{|Z_{reco}-Z_{true}|}{|Z_{seed}-Z_{true}|} = 0.33$ and event 0 has a ratio of $\frac{|Z_{reco}-Z_{true}|}{|Z_{seed}-Z_{true}|} = 0.13$ so the z reconstruction is better than the seed in both events. The left column **(A)** and **(C)** show the likelihood scan for event 4 using the truth and reconstruction as fixed parameters respectively. The landscape has the same shape but shows much larger fluctuations in **(C)** as well as a higher -LLH. Despite the fluctuations and the "poor" seed, the minimizer is able to reconstruct a value close to the truth. The right column **(B)** and **(D)** show the likelihood scan for event 0 using the truth and reconstruction as fixed parameters respectively. Here the landscape i z looks really great and even though the seed is a bit worse than for event 4, the minimizer is able to reconstruct z even better. The -LLH value is also the same for the minimum in both **(B)** and **(D)**. This is the textbook example that would be amazing to see in all parameters.

Chapter 7

Conclusion

It has in this work been shown that the reconstruction method, DirectReco, is a viable method to reconstruct the physical parameters of simulated events in the IceCube Detector. There are however still some fundamental issues that need to be studied thoroughly before being a competitive reconstruction method compared to table look-up.
The investigation of the lower level simulation showed the assumption of noise- and PMT-simulation effectively canceling out in DirectReco to be false. The PMT simulation also showed issues with saturation in DOMs receiving an overflow of photons. This is the first time we've seen that here at NBI. Extremely weird behaviour in the PMT simulation as well, showed afterpulses occurring before prepulses. By removing this from the simulation along with addressing the known time binning issues in Millipede made the optimal Millipede hypothesis match the MC simulated data. The time binning was resolved by using logarithmic binning. This binning method preserves higher statistics in the tails of the waveforms, while maintaining time resolution at the waveforms, important for reconstruction of some of the parameters.
Scans of the likelihood landscape in energy showed a large improvement in reaching a smooth likelihood landscape at an oversampling value as low as one thousand. This was achieved by changing the time binning method from uniform to logarithmic time binning. However, scans of the likelihood landscape done by fixing the parameters not being scanned. to their true and reconstructed value respectively showed some strong disagreement. This is a concern as the reconstruction relies on the minimizer's ability to navigate the likelihood landscape properly before optimally end up finding the global minimum at the true value.
The focus in this work was on improving the performance of the energy reconstruction. The reconstruction method still shows a bias reconstructing towards energies higher than the truth. Analysis of the reconstruction performance and seed only showed a slight improvement from the seed to the reconstruction. In the energy reconstruction $\sim$ 50% of the reconstructed events failed to improve the seed value. Further analysis showed the minimizer to have a bias towards reconstructing a value higher than the initial seed. This is especially problematic when the seed value is higher that the truth. This was seen even after fixing the parameters, time and θ_{zenith} to their respective truth values thereby providing the optimal condition for a good energy reconstruction.
The remaining parameters, x,y,z and $\phi_{azimuth}$ was showed to reconstruct very well. Especially the z reconstruction was a prime example.

Much of the analysis on the energy reconstruction shows issues concerning the likelihood landscape and the minimizer's ability to navigate this landscape properly. These are the main steps that should be taken into account when further development, on reconstructing low energy events in DirectReco, starts.

Appendix A

Reconstruction of X,Y,Z,ϕ

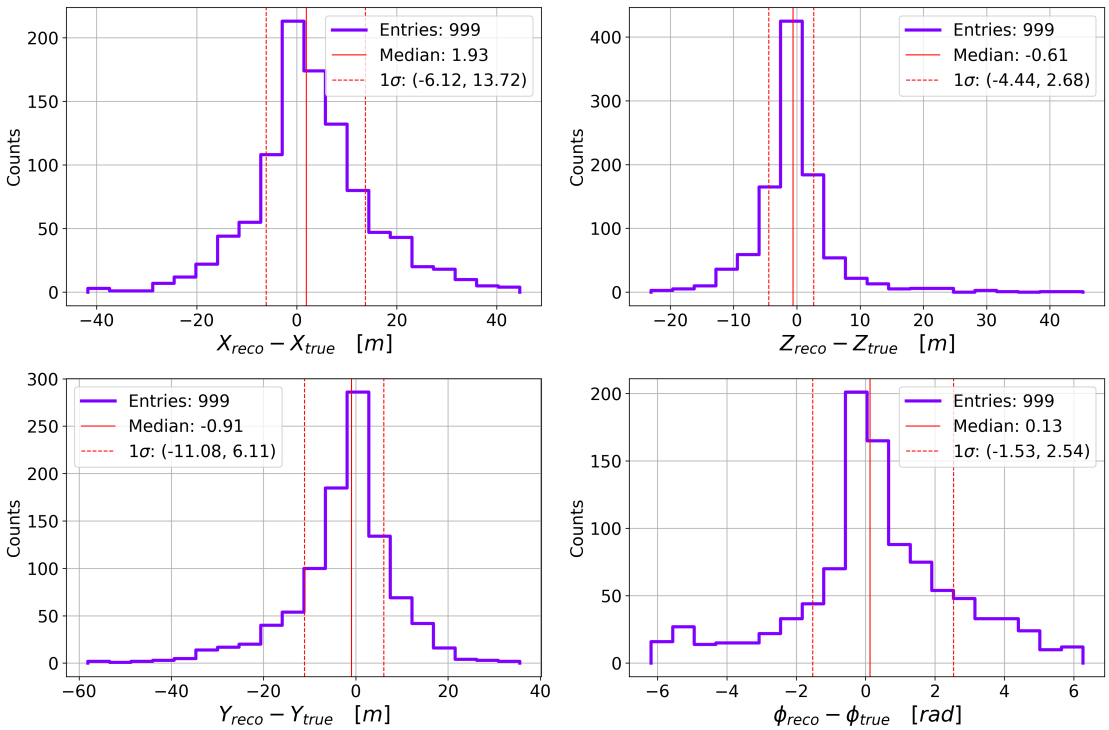

FIGURE A.1: The performance of reconstruction of X,Y,Z and azimuth angle. The distributions are show in purple. The red lines are the medians and the dashed red lines show the $\pm 1\sigma$ from the medians.

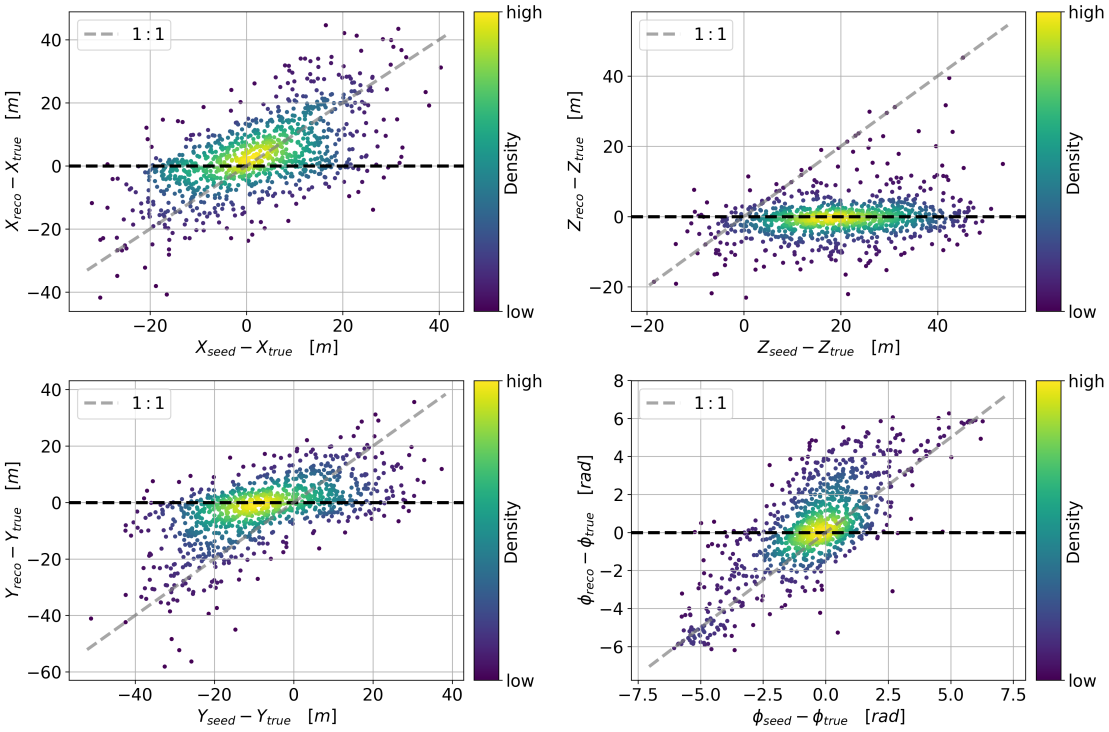

FIGURE A.2: Scatterplots of the error on the reconstructed values vs. the error on the seeded values. The grey dashed lines are the 1 : 1 lines where the errors match.

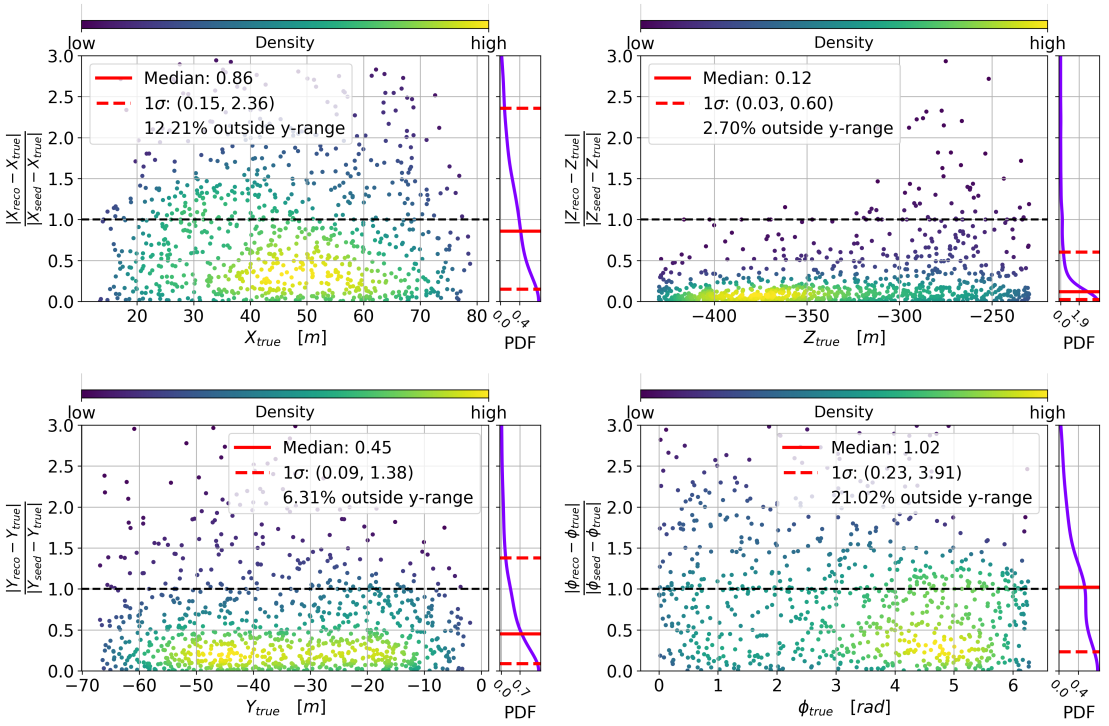

FIGURE A.3: Scatterplot of the ratio of the absolute distance between the reconstructed values and truth and the absolute distance between seed and truth vs. true energy. Events below the black dashed line reconstructs closer to the truth than the seeded value and vice versa. On the right of each plot the distribution of the ratio is shown.

Appendix B

Energy Seed

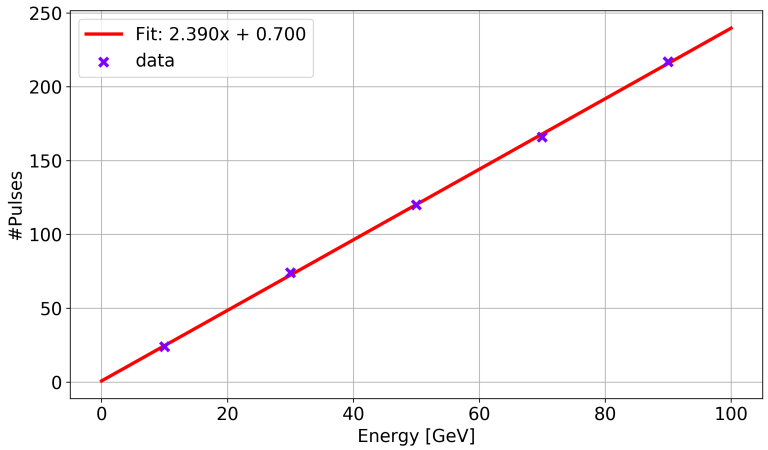

FIGURE B.1: Purple points are the mean number of pulses for 999 events at the corresponding energy. Red line is a 1D polynomial fit given the linear relationship between number of pulses and energy deposited is the detector.

The energy seeding is made by exploiting the linear relationship between the energy deposited and the amount of pulses in a given event. Inverting a 1D polynomial fit gives the energy used as seeding. To make the fit, 999 e^- was simulated using the distributions described above at energies of 10, 30, 50, 70 and 90 GeV. For each energy the mean amount of pulses pr event ($\#pulses$) was used a point and a straight line fit was done giving:

$$\#pulses = m \cdot energy + c \rightarrow energy = (\#pulses - c)/m \tag{B.1}$$

where the RHS of Equation B.1 is used as the energy seed after extracting the number of pulses the event the needs to be reconstructed. The fitted parameters are $m = 2.3899$ and $c = 0.7$. The fit and data points are shown in Figure B.1.

Bibliography

[1] W. Pauli. "Dear radioactive ladies and gentlemen". In: *Phys. Today* 31N9 (1978), p. 27.

[2] M.G. Aartsen et al. "Determining neutrino oscillation parameters from atmospheric muon neutrino disappearance with three years of IceCube DeepCore data". In: *Physical Review D* 91.7 (2015). ISSN: 1550-2368. DOI: 10.1103/physrevd.91.072004. URL: http://dx.doi.org/10.1103/PhysRevD.91.072004.

[3] M.G. Aartsen et al. "Measurement of atmospheric tau neutrino appearance with IceCube DeepCore". In: *Physical Review D* 99.3 (2019). ISSN: 2470-0029. DOI: 10.1103/physrevd.99.032007. URL: http://dx.doi.org/10.1103/PhysRevD.99.032007.

[4] M.G. Aartsen et al. "Observation of High-Energy Astrophysical Neutrinos in Three Years of IceCube Data". In: *Physical Review Letters* 113.10 (2014). ISSN: 1079-7114. DOI: 10.1103/physrevlett.113.101101. URL: http://dx.doi.org/10.1103/PhysRevLett.113.101101.

[5] R. Abbasi et al. "FIRST NEUTRINO POINT-SOURCE RESULTS FROM THE 22 STRING ICECUBE DETECTOR". In: *The Astrophysical Journal* 701.1 (2009), L47–L51. ISSN: 1538-4357. DOI: 10.1088/0004-637x/701/1/l47. URL: http://dx.doi.org/10.1088/0004-637X/701/1/L47.

[6] Mark Aartsen et al. "Multimessenger observations of a flaring blazar coincident with high-energy neutrino IceCube-170922A". In: *Science* 361.6398 (2018), eaat1378. ISSN: 1095-9203. DOI: 10.1126/science.aat1378. URL: http://dx.doi.org/10.1126/science.aat1378.

[7] M.G. Aartsen, R. Abbasi, and et al. "Detection of a particle shower at the Glashow resonance with IceCube". In: *Nature* 591.220-224 (2021). DOI: https://doi.org/10.1038/s41586-021-03256-1.

[8] B.R.Martin. *Nuclear and Particle Physics, An Introduction*. 2nd ed. John Wiley Sons Ltd, 2012. ISBN: 978-0-470-74275-4.

[9] URL: http://hyperphysics.phy-astr.gsu.edu/hbase/Particles/imgpar/neutleft.gif (visited on 05/15/2021).

[10] Ziro Maki, Masami Nakagawa, and Shoichi Sakata. "Remarks on the unified model of elementary particles". In: *Progress of Theoretical Physics* 28.5 (1962), pp. 870–880.

[11] Yoshiyuki Fukuda et al. "Evidence for oscillation of atmospheric neutrinos". In: *Physical Review Letters* 81.8 (1998), p. 1562.

[12] A. Bellerive et al. "The Sudbury Neutrino Observatory". In: *Nuclear Physics B* 908 (2016), 30–51. ISSN: 0550-3213. DOI: 10.1016/j.nuclphysb.2016.04.035. URL: http://dx.doi.org/10.1016/j.nuclphysb.2016.04.035.

[13] Marius Wallraff and Christopher Wiebusch. "Calculation of oscillation probabilities of atmospheric neutrinos using nuCraft". In: *Computer Physics Communications* 197 (2015), pp. 185–189.

[14] Pablo Fernández de Salas et al. "Status of neutrino oscillations 2018: 3σ hint for normal mass ordering and improved CP sensitivity". In: *Physics Letters B* 782 (2018), pp. 633–640.

[15] R. Abbasi et al. "The design and performance of IceCube DeepCore". In: *Astroparticle Physics* 35.10 (2012), 615–624. ISSN: 0927-6505. DOI: 10.1016/j.astropartphys.2012.01.004. URL: http://dx.doi.org/10.1016/j.astropartphys.2012.01.004.

[16] URL: https://www.jeol.co.jp/en/words/emterms/glossary_file/file/cherenkov-radiation_01.jpg (visited on 04/17/2021).

[17] Mark G Aartsen et al. "Energy reconstruction methods in the IceCube neutrino telescope". In: *Journal of Instrumentation* 9.03 (2014), P03009.

[18] Mark G Aartsen et al. "The IceCube Neutrino Observatory: instrumentation and online systems". In: *Journal of Instrumentation* 12.03 (2017), P03012.

[19] Markus Ahlers, Klaus Helbing, and Carlos Pérez de los Heros. "Probing particle physics with IceCube". In: *The European Physical Journal C* 78.11 (2018), pp. 1–51.

[20] URL: https://wiki.icecube.wisc.edu/index.php/File:DOM-Picture.png (visited on 04/26/2021).

[21] URL: http://www.psl.wisc.edu/services/electrical/dom (visited on 04/26/2021).

[22] URL: https://wiki.icecube.wisc.edu/index.php/File:PMT-Shematic.png (visited on 04/26/2021).

[23] Rasha Abbasi et al. "The IceCube data acquisition system: Signal capture, digitization, and timestamping". In: *Nuclear Instruments and Methods in Physics Research Section A: Accelerators, Spectrometers, Detectors and Associated Equipment* 601.3 (2009), pp. 294–316.

[24] URL: https://wiki.icecube.wisc.edu/index.php/Hard_Local_Coincidence (visited on 04/26/2021).

[25] URL: https://www.nbi.ku.dk/english/research/experimental-particle-physics/icecube/neutrino-oscillation/ (visited on 05/04/2021).

[26] Dmitry Chirkin. "Likelihood description for comparing data with simulation of limited statistics". In: *arXiv preprint arXiv:1304.0735* (2013).

[27] Alexander Lyle Wallace. "Direction reconstruction of IceCube neutrino events with millipede". PhD thesis. 2016.

[28] George B Dantzig. "Reminiscences about the origins of linear programming". In: *Mathematical Programming The State of the Art*. Springer, 1983, pp. 78–86.

[29] URL: http://www.scholarpedia.org/article/Nelder-Mead_algorithm (visited on 05/04/2021).

[30] C. Andreopoulos et al. "The GENIE neutrino Monte Carlo generator". In: *Nuclear Instruments and Methods in Physics Research Section A: Accelerators, Spectrometers, Detectors and Associated Equipment* 614.1 (2010), 87–104. ISSN: 0168-9002. DOI: 10.1016/j.nima.2009.12.009. URL: http://dx.doi.org/10.1016/j.nima.2009.12.009.

[31] MG Aartsen et al. "In-situ calibration of the single-photoelectron charge response of the IceCube photomultiplier tubes". In: *Journal of Instrumentation* 15.06 (2020), P06032.

[32] Halberg Thomas S. "Low Energy Neutrino Reconstructionin IceCube and the ICU". 2019. URL: https://www.nbi.ku.dk/english/research/experimental-particle-physics/icecube/group_theses/MastersThesis_ThomasH.pdf.

[33] Aya Ishihara. *The IceCube Upgrade – Design and Science Goals*. 2019. arXiv: 1908.09441 [astro-ph.HE].